Catalysis Science & Technology

ROYAL SOCIETY OF CHEMISTRY

PAPER

View Article Online
View Journal | View Issue

Cite this: *Catal. Sci. Technol.*, 2025, **15**, 5150

Modelling hydrogen peroxide adsorption on cerium dioxide: the effect of surface strain†

Sidra Munir,* Thomas Smith, Khoa Minh Ta, Lisa J. Gillie, David J. Cooke and Marco Molinari *

Ceria nanoparticles are nanozymes that can serve as important biomedical tools mimicking enzymes. The main issue with using metal oxide nanoparticles is the control of their surface speciation, which ultimately affects catalytic activity. Herein, we employ density functional theory calculations to unravel the adsorption of hydrogen peroxide and its dissociation products (hydroxyl, peroxide, superoxide and hydroperoxide) and the effect of strain on the absorption. Indeed, all nanoparticles are affected by intrinsic strain. We found that molecular H_2O_2 is unstable on the {100} surface at all strains, whereas hydroxyl radicals can be stabilized on reduced surfaces because of the electron transfer from surface Ce^{3+}. Upon dissociation, the peroxide ion is not always the most stable adsorbed species on all surfaces, whether strained, unstrained, stoichiometric or reduced, and superoxide species may also occur under tensile strains. Our thermodynamic methodology connects atomic-level findings to particle morphology in relation to environmental factors such as temperature and vapor pressure. Regardless of the strain applied, the adsorption of hydrogen peroxide and its dissociation products fails to access nanoparticle shapes other than octahedral, which is not ideal for peroxidase activity considering the characteristics of the {111} surface which is less effective in anchoring the adsorbed species.

Received 16th May 2025,
Accepted 14th July 2025

DOI: 10.1039/d5cy00589b

rsc.li/catalysis

1. Introduction

Cerium oxide nanoparticles (CeNPs, nanoceria) are materials of significant interest in catalysis,[1] environmental science,[2] biological technologies,[3–8] and many other applications.[9] The oxygen storage capacity (OSC) and redox behaviour of nanoceria are key to these applications. CeNPs can shuttle between Ce(III) and Ce(IV) oxidation states, forming oxygen defects during reduction and healing them during oxidation.[10,11]

CeNPs are promising artificial nanoscale enzymes (nanozymes) with multi-antioxidant enzyme mimicking and reactive oxygen species (ROS) buffering activities. Such activities are affected by temperature, pH, nanocrystal sizes and the Ce(III)/Ce(IV) ratio.[12–15] Nanoceria has been shown to mimic catalase (CAT),[16] oxidase (OXD),[17] peroxidase (POD),[18] and superoxide dismutase (SOD).[10,19] Under acidic conditions, ceria shows pro-oxidant activities (*e.g.* OXD and POD) and anti-oxidant activities under neutral or alkaline conditions (*e.g.* SOD and CAT).[20,21]

ROS, such as hydrogen peroxide (H_2O_2), hydroxyl radicals (·OH) and superoxide ($O_2^{\cdot-}$), are important species involved in various biological processes, such as cell signalling and antimicrobial defence. However, in excess, ROS can disrupt these biological processes and cause oxidative stress, which underlies neurological and cardiovascular diseases.[22] Thus, the need to develop novel antioxidant (or oxidant) nanozymes with high therapeutic efficiency is essential.[6] As scavengers, CeNPs have been used to counteract oxidative stress-mediated disorders.[23,24]

Significant attention has been given to the interactions between nanoceria and H_2O_2.[9,25] While the superoxide anion may cause more oxidative damage directly, hydrogen peroxide is considered to produce more harmful radicals owing to its greater oxidative potential. Indeed, CeNPs produce H_2O_2 while acting as SOD nanozymes.[19] Excess H_2O_2 may undergo Fenton-like reactions, generating hydroxyl radicals (·OH).[26] Computational efforts to determine the underlying mechanisms of SOD, CAT and POD mimetic activities of nanoceria have been proposed.[7,27]

Strain is a factor that can tune catalytic activity. Strain can be introduced chemically through the reduction of Ce^{4+} to Ce^{3+}, as Ce^{3+} has a larger ionic radius than Ce^{4+},[28] and *via* doping, where Ce ions are substituted with smaller or larger cations.[29–31] Lattice strain can also be used to tune the buffering activity of ceria towards ROS; however, it is a

Department of Physical and Life Sciences, University of Huddersfield, Queensgate, Huddersfield HD1 3DH, UK. E-mail: sidra.munir@hud.ac.uk, m.molinari@hud.ac.uk

† Electronic supplementary information (ESI) available. See DOI: https://doi.org/10.1039/d5cy00589b

relatively novel approach. For example, traversing the nanoscale has shown that ultrathin CeO_2 nanoplates with 3% intrinsic in-plane and 10% out-of-plane tensile strain display a ~2.6 increase in SOD activity compared to unstrained ceria.[32]

Core@shell nanomaterials can introduce surface strain effects and improve nanozymatic activity. In Fe_3O_4@CeO_2 NPs, the proximity of Fe_3O_4, which acts as POD converting H_2O_2 to ·OH, and of CeO_2, which acts as SOD converting $O_2^{\cdot-}$ to ·OH, allows for consecutive reactions where ·OH radicals are continuously generated compared to the two individual materials, resulting in the apoptosis of acute myeloid leukemia cells.[33] Substantial hybridization between TiO_2 and CeO_2 in CeO_2@TiO_2 stabilizes the Ce^{3+} sites at the interface, preventing their oxidation to Ce^{4+}, with the hybridization of the Ce 4f and the O 2p bands of TiO_2 in turn increasing POD activity of the composite material.[34] The POD activity of Cu_2-O@CeO_2 (ref. 35) and Co_3O_4@CeO_2 hybrid microspheres[36] exhibited strong POD activity due to interfacial interaction between the core and shell materials and an increase in the Ce^{3+}/Ce^{4+} ratio and oxygen vacancy concentration.

Several complex composite nanoparticles have been synthesized, including GO@SiO_2@CeO_2 hybrid nanosheets, which possess intrinsic POD activity and are used for non-toxic detection of H_2O_2.[37] Au@CeO_2 shows excellent pH-controlled CAT, POD and SOD activities at temperatures up to 90 °C and pH in the range of 2–11.[38]

The direct experimental measurement of structural changes due to lattice and mechanical strain is challenging;[39] however, computer simulations can help address changes at the atomistic level and relate them to surface properties.[40] Here, our overarching goal is to define the behaviour of ceria under compressive and tensile strain and how this affects the interaction of ROS with ceria surfaces. Specifically, we present a density functional theory study on the adsorption of H_2O_2 and its dissociation products on CeO_2 surfaces. We then use a thermodynamic approach to determine the temperature at which these species would desorb and the impact of adsorption on the thermodynamic morphology of ceria nanoparticles.

2. Methodology

Density functional theory (DFT+U) calculations were performed using the Vienna *Ab initio* Simulation Package (VASP) code.[41] A plane wave basis set with a cut-off energy of 500 eV was used with the projector augmented wave (PAW)[42] pseudopotentials to represent the interactions between the valence and core electrons. The exchange correlation functional used is the Perdew-Burke-Ernzerhof generalised gradient approximation (GGA, PBE).[43] The Hubbard correction parameter (U_{eff} = 5 eV) is included using the Dudarev approach.[44] This enables the localization of the 4f Ce electrons and has been successfully employed previously.[45–51]

The isolated H_2O_2 and O_2 molecules were modelled at the Γ-point in a cubic cell of 1000 Å^3. The minimized bulk structures for CeO_2 and Ce_2O_3 were taken from our previous work, which was used for the construction of surface models.[40,52] However, we provide a brief summary here for clarity. The CeO_2 {100}, {110} and {111} surfaces were obtained from bulk CeO_2 using the METADISE code.[53] The slab method was used,[54] which provides identical surfaces at the top and bottom of the slab. The slabs were expanded by $\sqrt{2}\times\sqrt{2}$ for {100} and {111} surfaces and by $2\times\sqrt{2}$ for the {110} surface. The {100} and {110} slabs are seven layers thick (28 CeO_2 units) and the {111} slab is five layers thick (20 CeO_2 units). The dipole moment normal to the polar {100} surface is removed by moving half of the oxygen atoms from the bottom to the top layer of the slab.[55] A vacuum gap of 15 Å was introduced perpendicular to the surface plane to ensure no image interactions. Our calculations do not account for possible reconstructions of the surfaces. Our stoichiometric surfaces represent models for oxygen-rich conditions, which are likely to favour the O-t reconstruction instead of the CeO_4-t reconstruction. Furthermore, the energy difference between the two reconstructions is relatively small.[56] Reduced surfaces (oxygen-deficient surfaces) were created by removing a surface oxygen atom symmetrically on the top and bottom layers of the slab. The two electrons introduced by the removal of an oxygen atom are localized on two Ce^{4+}, reducing them to two Ce^{3+}. Although it is possible to account for different locations of Ce^{3+} on O-deficient surfaces, using, for example, the occupation-matrix control, there is an added computational cost that has not been considered here.[57]

For the surface models, the Brillouin zone was sampled using a Monkhorst–Pack Γ-centred k-point mesh with a 2 × 2 × 1 mesh, with electronic and ionic convergence criteria of 10^{-6} eV per atom and 10^{-2} eV Å^{-1}, respectively.

Hydrogen peroxide can be adsorbed molecularly as H_2O_2 or dissociatively in three different configurations, *i.e.*, H/OO/H, H/OOH/, and HO/OH. The adsorption configurations of H_2O_2, H/OO/H, H/OOH/, and HO/OH adsorbed on unstrained stoichiometric and O-deficient surfaces are taken from our previous work;[23] however, their energies have been recalculated using the current calculation settings. We have not considered the effect of coverage in our models as this would increase complexity as multiple adsorbates could adsorb in different forms (*i.e.*, molecular and dissociative within the same model), thereby increasing the complexity of the configurational landscape. Furthermore, the current adsorption models do not account for the aqueous environment, neither explicitly nor implicitly; therefore, the effect of pH in our calculation is not considered.

When applying strain to our surface models, only the surface plane is subjected to an isotropic biaxial strain. In 1% intervals, strain values range from +4% (tensile) to −4% (compressive). We use labels, such as X%_^{58}Y-Z, where X% is the strain in percentage,[58] are the Miller index of the surface, Y is either S for stoichiometric or R for reduced (oxygen deficient) surfaces, and Z is the nature of the hydrogen peroxide adsorbed in the

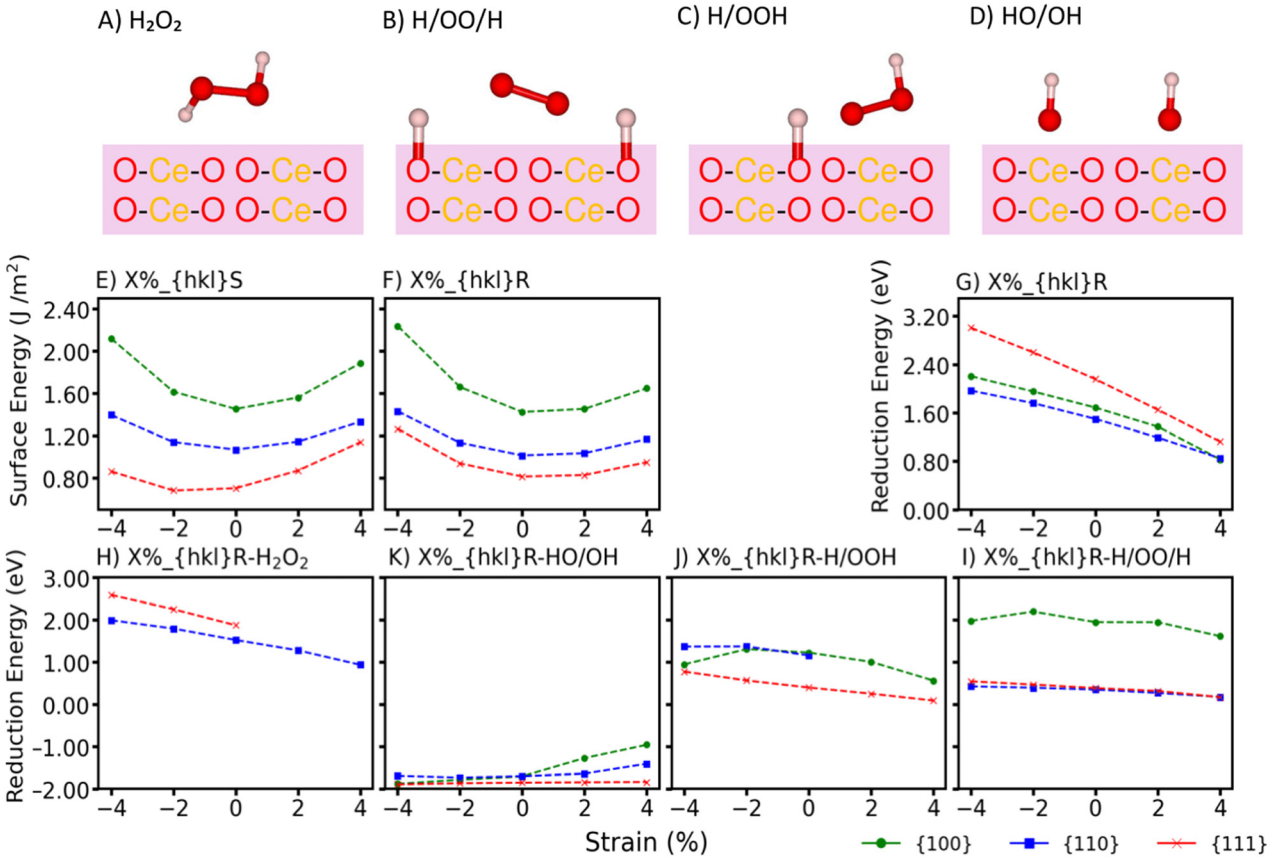

Fig. 1 Schematics of (A) molecular H_2O_2 and dissociative (B) H/OO/H, (C) H/OOH, and (D) HO/OH adsorption states on ceria surfaces. Surface energies of (E) stoichiometric and (F) reduced CeO_2 under compression (negative) and tensile (positive) strain. Reduction energies of reduced CeO_2 surfaces as a function of strain: (G) bare; (H) molecular H_2O_2; and dissociative (I) H/OO/H, (J) H/OOH and (K) HO/OH hydrogen peroxide.

molecular H_2O_2 and dissociative H/OO/H, H/OOH, HO/OH states. All four adsorption states are considered on both stoichiometric and oxygen-deficient surfaces and are schematically represented in Fig. 1A–D. All configurations are schematically reproduced in Fig. S1–S3.† All attempts to stabilize the *X*%_{100}R-H_2O_2 configurations were unsuccessful at all strain values considered, where molecular H_2O_2 dissociated spontaneously. We were also unable to stabilize 2%_{110}R-H/OOH, 4%_{110}R-H/OOH, 2%_{111}R-H_2O_2, and 4%_{111}R-H_2O_2, where all species dissociated spontaneously.

3. Results and discussion

3.1. The energetics of ceria surfaces

The surface energy of bare surfaces, γ_{Bare}, determines the stability of surfaces according to eqn (1).

$$\gamma_{Bare} = \frac{1}{2A}\left\{E_{Slab,Bare} - \left[(n_{CeO_2} - 2n_v)E_{Bulk,CeO_2} + n_v E_{Bulk,Ce_2O_3}\right]\right\} \quad (1)$$

$E_{Slab,Bare}$ is the energy of a slab either a bare stoichiometric $E^{Stoich}_{Slab,Bare}$ or a bare oxygen-deficient $E^{O\text{-}Def}_{Slab,Bare}$ slab. The surface area is A, which is multiplied by 2 to account for the symmetrical top and bottom surfaces of the slab. n_{CeO_2} is the number of CeO_2 formula units and n_v is the number of oxygen vacancies. E_{Bulk,CeO_2} and E_{Bulk,Ce_2O_3} are the energies per formula unit of the unstrained bulk structures CeO_2 and Ce_2O_3, respectively.

The surface energies of unstrained {100}, {110} and {111} stoichiometric[40,41,45–47,61] and oxygen-deficient[52] CeO_2 surfaces are consistent with the literature (Table S1† for a detailed comparison). The {111} is the most stable surface, and the trend of stability follows the order {111} > {110} > {100} for both stoichiometric and O-deficient surfaces (Fig. 1E and F). Compressive and tensile strain destabilise all three stoichiometric (Fig. 1E) and O-deficient (Fig. 1F) surfaces, as the strain increases and decreases the length of Ce–O bonds, resulting in weaker and stronger overlaps of O 2p and Ce 5d/4f states, respectively.[62]

The reduction energy (E_{redu}, eqn (2)) is the energy required to form a surface oxygen vacancy and reduce ceria surfaces.

$$E_{redu} = \frac{\left(E^{O\text{-}Def}_{Slab} + E_{O_2}\right) - E^{Stoich}_{Slab}}{2} \quad (2)$$

$E^{O\text{-}Def}_{Slab}$ and E^{Stoich}_{Slab} are the energies of the oxygen-deficient and stoichiometric surfaces, either strained or unstrained, either bare ($E^{O\text{-}Def}_{Slab,Bare}$ and $E^{Stoich}_{Slab,Bare}$) or adsorbed with hydrogen peroxide ($E^{O\text{-}Def}_{Slab,Ads}$ and $E^{Stoich}_{Slab,Ads}$). E_{O_2} is the energy of the

Table 1 The reduction energy (eV) of the {111} strained CeO_2 surfaces compared with literature values

E_{redu} (eV) of X%_{111}R					
Strain (%)	−4	−2	0	2	4
This work, PBE+U (U = 5 eV, $\sqrt{2}\times\sqrt{2}$)	3.0	2.59	2.15	1.65	1.12
PBE+U (U = 4.5 eV, 2 × 2)[59]	3.20	2.84	2.37	1.88	1.37
PBE+U (U = 5 eV, 2 × 2)[60]	3.43	2.87	2.30	1.79	1.29
PBE+U (U = 5 eV, 5 × 5)[60]	3.13	2.67	2.11	1.49	0.91

oxygen molecule. The factor 2 accounts for the oxygen vacancies present on both sides of the slab model.

The order of reducibility of CeO_2 surfaces is {110} (1.49 eV) > {100} (1.68 eV) > {111} (2.15 eV), *i.e.*, it is easier to reduce the {110} surface in agreement with the literature.[63–65] Literature data for the reduction energies of unstrained surfaces are provided in Table S2,† while those for unstrained and strained {111} surfaces are shown in Table 1. Less positive values indicate that it is easier to form an oxygen vacancy on the surface. Tensile strain favours the formation of oxygen vacancies (Fig. 1G). This is most likely because under tensile strain, the cubic structure is able to accommodate the larger Ce^{3+} cations (ionic radii: Ce^{3+} 1.143 Å *vs.* Ce^{4+} 0.97 Å), thereby facilitating the structural relaxation of the surface.[62,66]

In the presence of H_2O_2, the order of reducibility of ceria surfaces is different for each mode of adsorption (H_2O_2, H/OO/H, H/OOH/, and HO/OH). We were unable to stabilize all configurations of molecularly adsorbed H_2O_2, as it spontaneously dissociated on the surfaces. This is particularly evident on the X%_{100}R-H_2O_2 surface, where none of the molecular configurations survived. This may be related to the activation energy of hydrogen dissociation from the hydrogen peroxide molecule, which is calculated to be five times lower on the reduced {100} surface than the {111} (0.16 *vs.* 0.75 eV).[67] However, we observed spontaneous dissociation of H_2O_2 on the {100} oxygen-deficient surfaces, both unstrained and strained, and on the tensile-strained {111}R surface (Fig. 1H).

For the different dissociated states of hydrogen peroxide (Fig. 1H–K), the order of reducibility exhibits a complex behaviour with distinct trends that are similar for all percentages of strain. The {111} surface is generally the easiest to reduce, competing with the {110} for H/OO/H (Fig. 1I). The {100} surface requires the highest energy to form an oxygen vacancy, competing with the {110} for the H/OOH (Fig. 1J). The reduction energy of ceria surfaces with adsorbed HO/OH is a peculiar case as they are negative (Fig. 1K). On stoichiometric surfaces, the cleavage of the peroxide O–O bond produces OH species of more of an anionic nature on the {100} and {110} surface and of a radical nature on the {111} surface, as the electron density is redistributed on the ceria oxygen sublattice.[68] By creating an oxygen vacancy, the O-deficient surfaces have two excess electrons localized on Ce^{3+}. When OH radicals adsorb on the O-deficient surfaces, they are reduced to hydroxyl OH anions, oxidising Ce^{3+} to Ce^{4+} ions. This process further stabilizes the O-deficient adsorbed surfaces and hence the reduction energies are negative. Inspection of all our O-deficient configurations reveals the presence of surface Ce^{3+} ions, which are not present when dissociated hydrogen peroxide in the HO/OH form is adsorbed. Cerium oxide nanoparticles can exhibit an increase in Ce^{3+} concentration when H_2O_2 adsorbs on their surface.[30] For the adsorption of H/OO/H on oxygen-deficient and stoichiometric surfaces, we see the formation of peroxo species; however, at higher tensile strains, a superoxo species is stabilized as well, with an increase in Ce^{3+} concentration. Tables S3–S18† provide details of the Ce^{3+} concentration and the nature of the ROS adsorbed on all our X%_{100}Y-Z, X%_{110}Y-Z and X%_{111}Y-Z surfaces. Cerium oxide can act as an antioxidant scavenger and an oxidant-producing reactive radical species. Thus, tensile strain can promote oxidant activity because it favours the production of more active ROS and an increase in surface Ce^{3+} species.

3.2. The adsorption of H_2O_2 and its dissociation products on stoichiometric and O-deficient CeO_2 surfaces

The adsorption energy, E_{Ads} (eqn (3)), on stoichiometric and oxygen-deficient CeO_2 surfaces, is calculated from the energy of the adsorbed surfaces, $E_{Slab,Ads}$, whether stoichiometric $E^{Stoich}_{Slab,Ads}$ or oxygen deficient $E^{O\text{-}Def}_{Slab,Ads}$, and the energy of bare surfaces, $E_{Slab,Bare}$, whether stoichiometric $E^{Stoich}_{Slab,Bare}$ or oxygen deficient $E^{O\text{-}Def}_{Slab,Bare}$. $E_{H_2O_2}$ is the energy of the hydrogen peroxide molecule, $n_{H_2O_2}$ is the number of adsorbed hydrogen peroxide species, and 2 accounts for the adsorption on the top and bottom of the slab.

$$E_{Ads} = \frac{E_{Slab,Ads} - \left(E_{Slab,Bare} + n_{H_2O_2}E_{H_2O_2}\right)}{2} \quad (3)$$

The calculated adsorption energies of H_2O_2 and its dissociation products (HO/OH, H/OOH, H/OO/H) on stoichiometric and reduced CeO_2 surfaces are shown in Fig. 2. The top view of all adsorption configurations on the {100}, {110} and {111} stoichiometric and reduced CeO_2 surfaces are presented in the ESI† (Fig. S1–S3).

For unstrained and strained stoichiometric and O-deficient surfaces, the adsorption stability of molecular H_2O_2 follows the order {110} > {100} > {111} (Fig. 2A and E – note that some configurations are not presented as they could not be stabilised). Our data indicate that molecular H_2O_2 interacts to a lesser extent with stoichiometric than oxygen-deficient {111} surfaces, which is consistent with the reported literature (Table 2).[68] The adsorption of H_2O_2 on oxygen-deficient surfaces is more stable than on stoichiometric surfaces.[68] However, we see that the

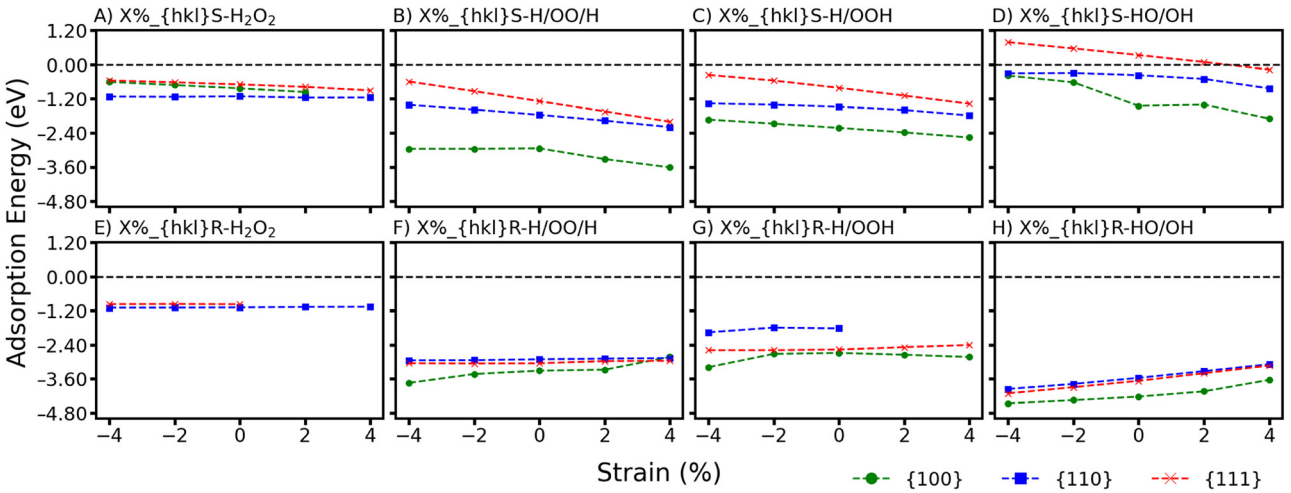

Fig. 2 Adsorption energy of H_2O_2 on stoichiometric/reduced CeO_2 {100}, {110}, and {111} surfaces as a function of strain: molecular (A and E) H_2O_2 and dissociative (B and F) H/OO/H, (C and G) H/OOH, and (D and H) HO/OH adsorption hydrogen peroxide.

adsorption of H_2O_2 on stoichiometric {110} is competitive to that on oxygen-deficient {110} surfaces across all compressive and tensile strains, with a minimal difference of −0.02 eV. The adsorption stability of molecular H_2O_2 remains unchanged upon applying compressive and tensile strain on ceria surfaces (Fig. 2A and E). However, we observe a small destabilization and stabilization when increasing compressive and tensile strain, respectively.

Stronger adsorption is observed in our study for 0%_{110}S-H_2O_2 (−1.11 eV), followed by 0%_{100}S-H_2O_2 (−0.83 eV) and 0%_{111}S-H_2O_2 (−0.69 eV). The most negative adsorption energy on the {110} stoichiometric surface is likely due to its open structure, with exposed surface Ce atoms, whereas the {111} and {100} surfaces are oxygen-terminated, with the {111} showing a tightly packed surface O layer.[69] Our data on molecular H_2O_2 adsorption on the stoichiometric {111} surface are in line with the literature (−0.75 eV using PBE+U = 4.5 eV,[70] and −0.70 eV using PBE+U = 3eV (ref. 69)). Our value for the adsorption of molecular H_2O_2 on the stoichiometric {110} surface is more negative than the literature-reported value (PBE+U = 5 eV, −0.85 eV (ref. 71)); this is due to the different configurations, with ours having both hydrogen atoms hydrogen-bonding the surface while the literature has only one hydrogen atom pointing down toward the surface.

The same trend is observed for 0%_{100}S-H_2O_2, where the literature reports a value of −0.25 eV (ref. 70) (PBE+U = 5 eV) compared to our value of −0.83 eV. However, this discrepancy is due to different surface terminations, with the literature reporting Ce-terminated surfaces while we studied O-terminated surfaces.

For the adsorption of H_2O_2 in its dissociative states, *i.e.*, H/OO/H, OH/OH and H/OOH, the adsorption stability on stoichiometric surfaces follows the order {100} > {110} > {111} (Fig. 2B–D), which is consistent with our previous work.[23,24] The least stable adsorption is the HO/OH on stoichiometric CeO_2. This is due to the inability of stoichiometric CeO_2 surfaces to oxidise further (*i.e.*, the intrinsic inability of Ce^{4+} to access higher oxidation states), reducing the formation of hydroxyl radicals. The adsorption of OH radicals on the stochiometric {111} surface is unstable (*i.e.*, the adsorption energy has a positive value) but can be stabilised on the {100} and {110} surfaces as hydroxyl anions (Fig. 2D).[39] Increasing the compressive/tensile strain destabilizes/stabilizes the adsorption of H/OO/H, H/OOH and HO/OH on all three surfaces (Fig. 2B–D).

The positive energy for the adsorption of dissociated H_2O_2 on the {111} stoichiometric as 0%_{111}S-HO/OH (0.33 eV), although lower, is in line with the literature (0.72 eV (ref. 68)). However, positive energies are not observed for the adsorption of one OH radical on the 0%_{111}S-OH surface (−1.0 eV), although this is contradictory, as the authors stated that this binding is thermodynamically unstable.[72] The {111} surface is oxygen-terminated and does not allow for a strong relaxation that could counteract the lack of further oxidation of surface cations; indeed, OH radicals cannot be quenched to become OH anions as there is no electron donor Ce^{3+} that could oxidise to Ce^{4+} (Table S16†). Such positive energies are not observed for the 0%_{100}S-HO/OH surface, which has a liquid-like behaviour[73] and on the 0%_{110}S-HO/OH, which has surface Ce species directly exposed to adsorbates. The adsorption energy changes significantly when it comes to the adsorption of H_2O_2 as HO/OH on all three oxygen-deficient surfaces. All energies are very negative, as the presence of Ce^{3+} due to oxygen vacancies can reduce OH radicals to anions.

The energy barrier for the dissociation of H_2O_2 to H/OOH on an unstrained {111} stoichiometric surface is low (0.09 eV); however, it results in a more stable adsorption of H/OOH (−0.96 eV) compared to H_2O_2 (−0.79 eV).[68] In our study, the hydroperoxo moiety (OOH) in 0%_{111}S-H/OOH has an adsorption energy of −0.81 eV, more stable than the molecular adsorption of H_2O_2 in 0%_{111}S-H_2O_2 (−0.69 eV). The differences between the two studies likely arise from the different functionals (PBE0 (ref. 68) *vs.* PBE+U in this study) and the size of the systems studied (9 atomic layers[68] *vs.* 15

Table 2 The adsorption energy (eV) of hydrogen peroxide in all adsorption states on stoichiometric and oxygen-deficient ceria surfaces

Surface label	Adsorption energy (eV) (this work and ref. 23)	Adsorption energy (eV) (literature)
0%_{111}S-H_2O_2	−0.69	−0.67,[87] −0.79,[68] −0.75,[70] −0.70 (ref. 69)
0%_{111}S-H/OO/H	−1.28	−0.60,[c,68] −0.56,[b,68] −0.47[a,68]
0%_{111}S-OO	—	−0.98,[c,75] (0.91–0.95),[d,75] (−0.05–0.002),[d,82] −0.04,[d,81] −0.01–−0.03[d,79]
0%_{111}S-H/OOH	−0.81	−0.96,[68] −0.8 (ref. 72)
0%_{111}S-OH/OH	0.33	0.72 (ref. 68)
0%_{111}S-OH	—	−1.0[e,72]
0%_{110}S-H_2O_2	−1.11	−0.85,[71] −1.10 (ref. 87)
0%_{110}S-H/OO/H	−1.76	—
0%_{110}S-OO	—	−0.92[b,83]
0%_{110}S-H/OOH	−1.47	−1.33 (ref. 69)
0%_{110}S-OOH	—	−1.08[a,71]
0%_{100}S-H_2O_2	−0.83	−0.25,[g,70] −0.96 (ref. 87)
0%_{100}S-H/OO/H	−2.94	−1.95 (ref. 69)
0%_{111}R-H_2O_2	−0.97	−1.03 (ref. 68)
0%_{111}R-H/OO/H	−3.05	—
0%_{111}R-OO	—	−2.74,[b,79] −2.47,[c,79] (−0.90–−3.95),[b,75] −1.34,[b,82] −1.42,[b,76] (−0.30–−0.38),[b,‡,80] (−2.55–−4.00),[c,75] −1.86,[c,82] −1.9,[c,76] −2.80,[c,‡,80] −3.25,[c,†,80] −1.72,[d,79] (−0.01–−0.09),[d,82] −1.17,[d,84] −0.03,[d,85] −3.47,[81] −0.17[b,79]
0%_{111}R-H/OOH	−2.56	—
0%_{111}R-OOH	—	−2.8[a,72]
0%_{111}R-OH/OH	−3.67	(−2.92–−2.59),[e,68] −4.42[f,68]
0%_{111}R-OH	—	−4.10 (ref. 72)
0%_{110}R-H/OO/H	−2.91	
0%_{110}R-OO	—	−2.05,[c,86] −1.10,[b,79] −2.61[c,79]
0%_{100}R-H/OO/H	−3.97	—
0%_{100}R-OO	—	−1.62,[b,76] −2.14,[c,76] −2.02[c,86]

[a] Adsorbed as an intermediate species. [b] Adsorbed as a superoxide ion. [c] Adsorbed as a peroxo ion. [d] Adsorbed as molecular O_2. [e] OH is adsorbed as a radical species. [f] OH is adsorbed as an ion. [g] Adsorbed on cerium-terminated surfaces. PBE0 (2 × 2),[68] PBE+U (U = 5 eV, (—)),[70] PBE+U (U = 3 eV, (—)),[69] PBE (2 × 2),[79] PBE+U (U = 5 eV, (3 × 2),[81] PW91 (—),[75] PW91+U (U = 7 eV, ($\sqrt{3}$ × 2)),[82] PBE+U (U = 5 eV, (4 × 4)),[72] PBE+U (U = 5 eV, (2 × 2)),[71] PBE+U (U = 5 eV, (3 × 2),[83] PBE+U (U = 4.5 eV, (2 × 2)),[76] PW91+U (U = 5 eV, (2$\sqrt{3}$ × 3),[‡] and (2 × $\sqrt{3}$)[†]),[80] PBE+U (U = 4.5 eV, (2 × 2)),[84] PBE+U (U = 5 eV, (3 × 3)),[85] PBE+U (U = 5 eV, (2 × 2) for {110} and (2 × 4) for {100}),[86] and PBE+U (U = 3.1 eV, (2 × 2) for {110},{100} and {111}).[87]

atomic layers in our study). A stronger adsorption energy of −1.33 eV is obtained on the 0%_{110}S-H/OOH using PBE+U (U = 3 eV (ref. 69)), which agrees well with our value of −1.47 eV. Such a difference is most likely due to our configuration having both H atoms of the H_2O_2 pointing towards instead of one.[69]

The cleavage of the O–O bond in H_2O_2 forms two OH radicals. In our study, the dissociated 0%_{110}S-HO/OH gives an adsorption energy of −0.36 eV; however, the adsorption of one OH on the stoichiometric {110} surface (PBE+U = 5 eV, −2.29 eV) yields a more negative adsorption energy.[70]

Our 0%_{100}S-H/OO/H surface (−2.94 eV) compares well with the reported 0%_{100}S-H/OO/H (−1.95 eV using PBE+U = 3 eV).[69] Unlike the literature configuration, where only 1 oxygen of the peroxo ion interacts with the surface,[69] our configuration is more stable as the peroxo ion is embedded completely into the oxygen surface layer, as this surface layer has a liquid-like behaviour and can rearrange dramatically to accommodate adsorbates.[73]

The transfer of H to the surface from the OOH moiety can result in the formation of peroxo on 0%_{111}S-H/OO/H (−0.60 eV (ref. 68)), which is generally less stable as compared to that of 0%_{111}S-H/OOH (−0.96 eV (ref. 68)). In our study, we observe an opposite trend where the O_2 species (we could only stabilize an O_2 triplet on this surface and not a peroxide ion) adsorbed on the 0%_{111}S-H/OO/H yields a more negative adsorption energy (−1.28 eV) than the hydroperoxide adsorbed on the 0%_{111}S-H/OOH (−0.81 eV). Our 0%_{111}S-H/OOH configuration aligns well with literature reports.[68] However, we find a more stable structure where the O_2 species interacts by means of H bonds with the adsorbed hydrogen atoms, whereas the literature reports the peroxo adsorbed directly onto a cerium surface atom, making it formally 9-fold coordinated.[69] Such peroxo species have been observed in bulk ceria, where the peroxo is constrained in a bulk matrix.[74] The adsorption of peroxo species on the stoichiometric {111} surface has been calculated with a positive energy of 0.98 eV (PW91+U = 7 eV), most likely because of the transfer of electrons from the surface to the O_2 molecule.[75] In our case, the presence of additional hydrogen atoms (0%_{111}S-H/OO/H) bypasses the electron transfer to the O_2 molecule, and the adsorption stability is further enhanced through hydrogen bonding (−1.28 eV) and the injection of electrons into the surface forming Ce^{3+}.

Superoxide can be formed from peroxides at elevated temperatures on $CeO_{2-x}(100)$[76] and has been observed experimentally on 1% tensile-strained nanoparticles expressing the {100} and {111} facets,[77] and computationally (PBE+U = 5 eV) on the edges of ceria octahedral NP (expressing {111} surfaces) supercharged with adsorbed oxygen molecules.[78] However, in all our configurations, superoxide is only stable under a tensile strain of 4%_{111}R-H/OO/H, 2–4%_{100}R-H/OO/H, 2–4%_{100}S-H/OO/H, which implies that tensile strain or highly undercoordinated surface atoms are necessary to stabilize this species. The adsorption energy of the O_2 molecule on unstrained stoichiometric {111} (−0.01 eV) and {110} (−0.03 eV) surfaces yields loosely stable adsorption energies. When injecting an electron into the system, O_2 transforms into a superoxide species with adsorption energies of −1.10 eV and −0.17 eV for {110} and {111}, respectively, using PBE+U = 5.55 eV.[79] Although we have similar configurations, we do not inject extra electrons in the structure and have strong adsorption energies for 0%_{110}S-H/OO/H (−1.76 eV as peroxide) and 0%_{111}S-H/OO/H (−1.28 eV although this is an O_2 triplet).

Comparing the energetics of the adsorption on reduced and stoichiometric ceria surfaces, reduced ceria surfaces are generally more favourable for the adsorption of dissociated H_2O_2 across all strains, as indicated by the adsorption energies in Table 2. This is because on the defective surface, H_2O_2 dissociation is an energetically downhill reaction, which is thermodynamically driven by the healing of O vacancies.[68]

H_2O_2 adsorbs on reduced 0%_{111}R-H_2O_2 with an adsorption energy of −0.97 eV and a similar adsorption configuration to that reported in the literature (−1.03 eV).[68]

The adsorption energies of H/OO/H, H/OOH and HO/OH on oxygen-deficient surfaces follow the order of stability as {100} > {111} > {110} (Fig. 2F–H). Unlike tensile strain (except for X%_{100}R-H/OOH, Fig. 2G), increasing compressive strain generally stabilizes all the dissociative species adsorbed on o-deficient surfaces. We see the healing of the vacancy as more energetic on all surfaces for all dissociative adsorption configurations compared to molecular H_2O_2 adsorption that can be stabilized near the oxygen vacancy (0%_{110}R-H_2O_2 and 0%_{111}R-H_2O_2). The interaction of HO/OH with O-deficient surfaces is the most stable compared to H/OOH and H/OO/H, as the OH radicals are quenched to OH anions at the expense of surface Ce^{3+} oxidizing to Ce^{4+}. This oxidation of reduced CeO_{2-x} upon the adsorption of OH radicals has been reported in the literature (Table 2).[23,24,68]

The O–O bond of H_2O_2 is broken down with an electron transfer to that of Ce^{3+}, forming two OH on the surface with an adsorption energy of 0%_{111}R-HO/OH as −4.42 eV,[68] comparable to our adsorption energy of −3.67 eV. The difference between our and reported literature values could be due to the use of different functionals (PBE0 *vs.* PBE+U = 5 eV) and a very thin nine atomic layer in their study against our 15 layer. Oxygen vacancies can indeed produce larger relaxations. Moreover, they fixed the three atomic layers at the bottom, whereas in our study, we allowed relaxation at both the top and bottom layers.[68]

We calculated the adsorption energies of H/OO/H on both unstrained and strained reduced ceria surfaces. In our study, the adsorption of peroxo species in 0%_{111}R-H/OO/H has a stable adsorption energy of −3.05 eV, in agreement with the literature data on the adsorption of peroxo ions on a partially reduced {111} surface (−3.25 eV)[80] (PW91+U = 5 eV). The difference between the two studies arises from the presence of hydrogen in our configuration. Moreover, the different orientations of the adsorbed peroxo affect the adsorption energies (−2.55–−4.00 eV) using PW91.[75] However, as the structures are not provided, it remains unclear which of the reported structures is directly comparable to ours.

3.3. Desorption temperature

We can relate adsorption energies to the temperature of desorption, which, in principle, could be measured experimentally. We determine the temperature of desorption (T_D) of hydrogen peroxide using the Surfinpy code,[88,89] which has been used effectively in previous studies.[40,45–47] T_D is defined as the temperature at which H_2O_2 desorbs from a CeO_2 surface at a defined partial pressure, thereby defining the phase boundary between the bare and the H_2O_2 adsorbed surfaces.

The surface energy of H_2O_2 adsorbed surfaces (γ_{Ads}) is calculated using eqn (4).

$$\gamma_{Ads} = \gamma_{Bare} + \frac{n_{Ads}}{2A}\left(G_{Ads,(T)} - RT\ln\left(\frac{p_{Ads}}{p^o}\right)\right) \quad (4)$$

γ_{Bare} is the surface energy of the bare CeO_2 surface (eqn (1)), $\frac{n_{Ads}}{2A}$ is the adsorption coverage where n_{Ads} is the number of adsorbates and A is the surface area, which is multiplied by a factor of two to account for the symmetrical top and bottom surfaces, R is the gas constant, T is the temperature, p_{Ads} and p^o are the partial pressures of the adsorbate selected and the standard partial pressure (1 bar), respectively. $G_{Ads,(T)}$ is the adsorption energy of the adsorbate as a function of temperature according to eqn (5).

$$G_{Ads,(T)} = \frac{E_{Slab}^{Stoich,Ads} - \left(E_{Slab}^{Stoich,Bare} + n_{H_2O_2}G_{H_2O_2,(T)}\right)}{n_{H_2O_2}} \quad (5)$$

The energy of hydrogen peroxide ($G_{Ads,(T)}$) as a function of temperature is calculated using eqn (6).

$$G_{H_2O_2,(T)} = E_{H_2O_2} - TS_{(T)} \quad (6)$$

$S_{(T)}$ is the experimental entropy of gaseous H_2O_2.[90] This approach only accounts for the entropic effects of gaseous phases, excluding those of solid phases. Furthermore, it does not account for any kinetic effects due to the dissociation of H_2O_2.

Fig. 3A and B shows the desorption temperature of dissociative and molecular adsorbed H_2O_2 on the unstrained stoichiometric and O-deficient CeO_2 surfaces at the chosen partial pressures of H_2O_2 ($p_{H_2O_2}$ = −12, 0). On average,

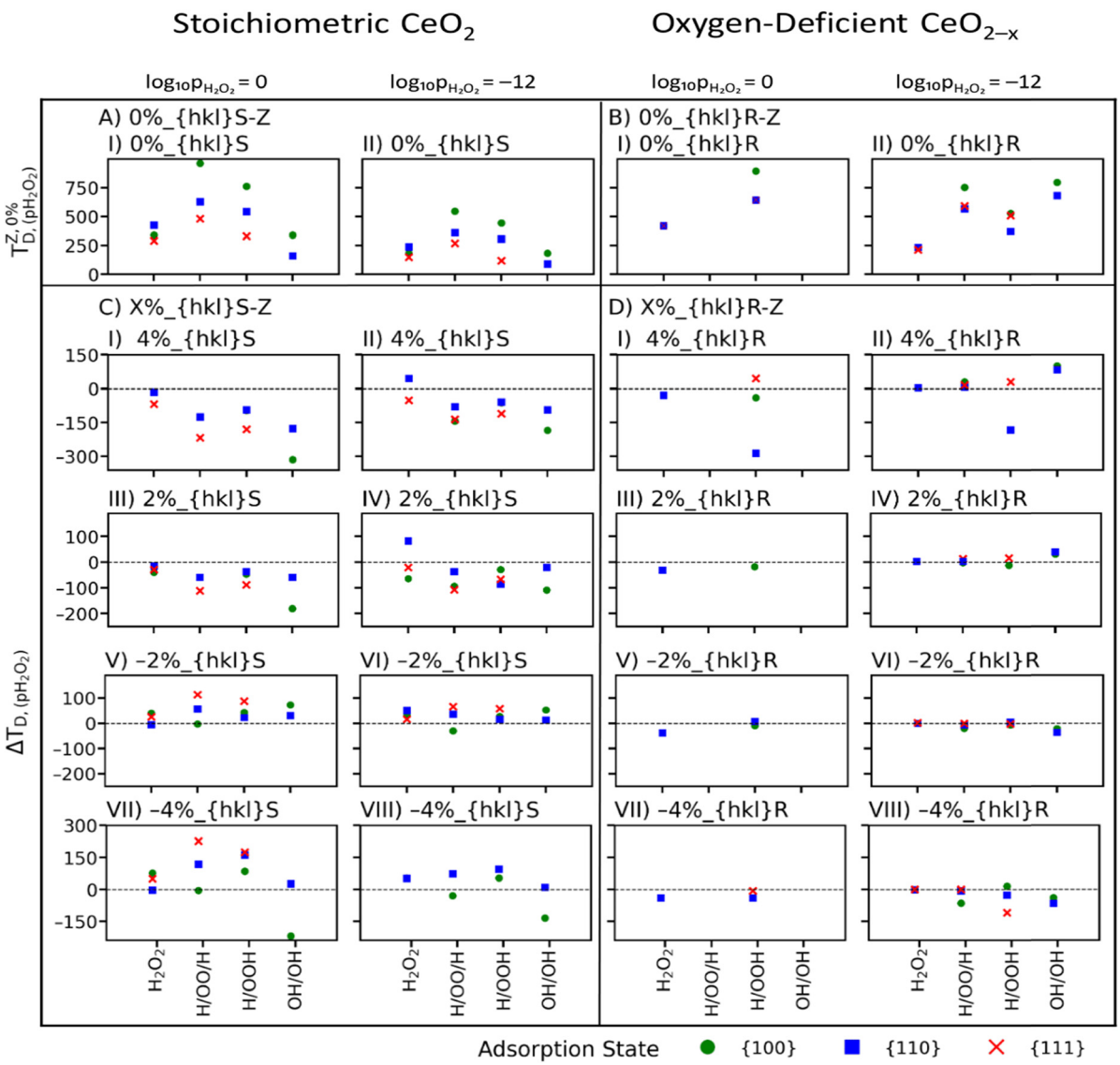

Fig. 3 Desorption temperature of molecularly and dissociatively adsorbed hydrogen peroxide on stoichiometric and oxygen-deficient CeO_2. $T^{N,0\%}_{D,(p_{H_2O_2})}$ of adsorbed hydrogen peroxide species on unstrained stoichiometric (A) and oxygen-deficient (B) CeO_2 surfaces. $\Delta T_{D,(p_{H_2O_2})}$ of adsorbed hydrogen peroxide species on strained stoichiometric (C) and oxygen-deficient (D) CeO_2 surfaces.

molecular H_2O_2 has lower T_D than dissociatively adsorbed H_2O_2. Molecular H_2O_2 desorbs at higher temperatures on {100} than {110} and {111} surfaces (Fig. 3A and B), and this behaviour is representative of the adsorption energies of molecular H_2O_2 on the surfaces, and in turn, of the strength of the interaction between hydrogen peroxide and ceria.

The limited literature regarding the desorption of H_2O_2 on ceria surfaces restricts comprehensive comparisons; however, we have included direct or indirect comparisons with analogous species, such as peroxo and superoxo species, wherever feasible.

The formation of (bridging or chelating) peroxide was detected using FTIR (1×10^{-5} Torr) on commercial CeO_2, where half of the adsorbed peroxide species were removed by 333 K and complete removal occurred by 363 K.[91] The interaction of CeNPs with H_2O_2 induced a colour change from yellow (CeO_2) to brown (CeO_2/H_2O_2), with the sample reverted to its original colour upon the removal of peroxide. Although not directly comparable, 0%_{100}S-H_2O_2, 0%_{110}S-H_2O_2 and 0%_{111}S-H_2O_2 show desorption temperatures of 338 K, 426 K, and 291 K at a pressure of 1.34×10^{-8} bar, respectively, while 0%_{110}R-H_2O_2 and 0%_{111}R-H_2O_2 show desorption temperatures of 419 K and 383 K, respectively.

The literature data concerning the adsorption of peroxide and superoxide on the ceria surface are rather complex, with a lack of agreement on the temperatures at which the desorption of peroxide and superoxide species is observed. While we do not investigate the adsorption of peroxide and superoxide as individual species, we adsorb hydrogen peroxide in its dissociated forms, H/OOH and H/OO/H, which are representative of the superoxide and peroxide species. We

observe the formation of peroxide on all our surfaces, independent of the applied strain and the stability of adsorption (Fig. 2). We were able to stabilize the superoxide (2–4%_{100}S-H/OO/H, 2–4%_{100}R-H/OO/H, 4%_{111}R-H/OO/H) in only a few cases (Tables S3–S18†).

Our oxygen species is stable at temperatures as low as 270 K for 0%_{111}S-H/OO/H (O_2 triplet), 361 K for 0%_{110}S-H/OO/H (peroxide) and as high as 574 K for 0%_{100}S-H/OO/H (peroxide) at 10^{-12} bar for stoichiometric unstrained surfaces. Our peroxide is stable at temperatures as low as 568 K for 0%_{110}R-H/OO/H, 593 K for 0%_{111}R-H/OO/H and as high as 751 K for 0%_{100}R-H/OO/H at 10^{-12} bar for unstrained oxygen-deficient surfaces. This is important as it displays variability in the range of desorption temperatures (as also seen in Fig. 3) and thus implies that more complex surface structural features may have even more different desorption temperatures. For the superoxide, the temperatures of desorption are within a 100 K difference depending on surface stoichiometry and tensile strain, *i.e.*, 640 K, 690 K, 722 K, and 752 K at 10^{-12} bar for the 2%_{100}S-H/OO/H, 4%_{100}S-H/OO/H, 2%_{100}R-H/OO/H, and 4%_{100}R-H/OO/H, respectively. These values remain well within the temperature range for the desorption of peroxide. Our calculated values are not directly comparable but display trends that are discussed hereafter.

The conversion between superoxide and peroxide was calculated with a migration barrier of 0.35 eV when adsorbed on a ceria {111} oxygen-deficient surface using PW91+U = 5 eV, indicating that superoxide might easily transform into peroxide with increasing temperature.[80] This was corroborated by FTIR measurements on weakly reduced ceria, where no peroxide was detected but superoxide was formed between 200 and 300 K and disappears at a temperature of 373 K.[92] On the other hand, on partially reduced ceria, both superoxide and peroxide were observed in the range of 200–373 K, with the superoxide progressively converted into the peroxide that persisted up to 420 K.[92] This implies that peroxide is the thermodynamically stable species, as evidenced by its prominence in our calculations, while superoxide represents a higher energy intermediate state when adsorbed onto ceria surfaces.

On cuboidal nanoceria expressing the {100} surface, an increase in temperature leads to a shift in the equilibrium between the peroxide and superoxide species, with the intensity of the *in situ* Raman band decreasing at 393 K for the peroxide and at 308 K for the superoxide.[76] This is corroborated by FT-IR spectroscopy on partially reduced ceria, where the peroxide is usually observed at a temperature higher than 373 K.[93] Such equilibrium is not seen on ceria nanosheets expressing the {111} surface, where the peroxide is the only species observed in the 333–393 K temperature range.[76] Using PBE+U (U_{eff} = 4.5 eV), the peroxide was calculated to be more stable than the superoxide species on the {100} surface (−2.5 *vs.* −1.83 eV), while the superoxide is more stable than the peroxide on the {111} surface (−1.42 *vs.* −0.91 eV).[76] According to our calculations, when hydrogen peroxide is adsorbed and dissociates on the {100} surface, only tensile strain can accommodate such superoxide species (*i.e.*, 2–4%_{100}S-H/OO/H, 2–4%_{100}R-H/OO/H). Furthermore, Raman spectroscopy showed that CeO_2 microflowers expressing {001} facets can stabilize O_2 as a peroxide species at room temperature and pressure, whereas spherical shapes can stabilize both superoxide and peroxide.[94] This would again imply that more complicated surface structures may be the key in stabilizing and tuning the equilibrium between the superoxide and peroxide.

Unlike on the {111} (surface [Ce^{3+}] = 45%), on the {110} ([Ce^{3+}] = 60%) and {100} ([Ce^{3+}] = 50%) reduced CeO_{2-x} surfaces, IRRAS spectroscopy (~8 × 10^{-11} mbar) revealed that the superoxide and peroxide coexists at 110 K with dissociation detected at above 160 K.[95] This is not consistent with *in situ* Raman spectroscopy results, which revealed that both species are observed at room temperature on the reduced {111} CeO_{2-x} surfaces.[75] Our data also suggest that these species may be present at much higher temperatures (Fig. 3).

O_2 could be adsorbed on reduced ceria but not on stoichiometric ceria as displayed by Raman spectroscopy.[96] However, on reduced ceria nanorods expressing {110} and {100} surfaces, superoxide is stable up to a temperature of 348 K as indicated by the disappearance of its Raman band; however, no superoxide is observed on nanocubes expressing {100} surfaces, and truncated nano-octahedra expressing {111} and {100} surfaces.[96] The peroxide is also stable on reduced nanorods and nanocubes but not nano-octahedra; however, the intensity of its Raman band decreases with increasing temperature to 473 K and 393 K, respectively, displaying that cuboidal NPs are less prone to stabilize the peroxide species compared to nanorods.[96] This could be related to the surface terminations of nanorods and nanocubes, where the surface Ce cations are more exposed on the {110} surface than on the oxygen-terminated {100} facets. Furthermore, this is corroborated by our findings that superoxide can be stabilized on strained surfaces and nanoparticles are intrinsically strained (Tables S3–S18†).

There is a debate on the desorption of superoxide ions below or above the room temperature on reduced ceria surfaces.[77,78,97] The DFT functional used in the simulations appears to have a significant impact on the calculated desorption temperatures for the superoxide ion. However, one must consider that such studies have investigated the adsorption of oxygen species on the edges of ceria nanoparticles, *i.e.*, highly undercoordinated sites.[97] For reduced octahedral CeO_{2-x} ($x \approx 0.18$–0.32) NPs with particle size 3–10 nm, PBE+U = 5 eV calculated the superoxide desorption at 184–199 K and HSE06 calculated the superoxide desorption at 415–429 K (with a larger value corresponding to smaller NPs).[97] Experimentally reduced ceria nanoparticles of size 8–13 nm with exposed {111} and {100} facets, and a measured 1% lattice strain on the {111} facet show a superoxide desorption temperature of 439 K using TPD (pressure not mentioned,[77] but generally TPD operates at UHV for peroxide detection[91]). However, the presence of superoxide was identified using EPR on reduced spherical ceria nanoparticles with a size <5 nm at much higher temperatures up to 675 K.[98] The

simulated reduced octahedral ceria NP expressing oxygen-deficient {111} surfaces using PBE+U = 6.2 eV, coupled with microkinetic modelled TPD, displayed a desorption signal for the superoxide ion at around 452 K.[78]

As oxygen adsorbs on the surfaces of ultra-small particles, this facilitates superoxo decoration, causing the nanoparticle to become supercharged. The NPs, rather than becoming stoichiometric by absorbing oxygen, stabilize themselves through oxygen chemisorption, forming superoxo ions due to electron transfer that occurs from the Ce^{3+} ions to the adsorbed O_2. The presence of superoxo ions was revealed using EPR at above RT and was observed in the temperature programmed reduction (TPR) spectrum in the range of 598–698 K for reduced octahedral ceria NPs expressing the {111} surface of sizes below 10 nm,[99] and at ~648 K for reduced truncated octahedral NPs of 3.7 nm with exposed {100} and {111} facets.[100] Our desorption temperatures for the adsorption of peroxide on 0%_111R_H/OO/H and 0%_100R_H/OO/H are 593 K and 751 K at 10^{-12} bar, which are close to the experimental values described above.

Nanorods expressing reduced {100} and {111} surfaces have a lower desorption temperature for the superoxide (407 K) compared to that of nanocubes expressing the {100} surfaces (421 K) and particles expressing the {100} and {111} surfaces (439 K). These nanoobjects are strained due to the presence of oxygen vacancies and Ce^{3+}, which is higher in rods and particles compared to cubes. Although cubes experience a lattice strain of 0.3% while rods and particles experience a strain of 1% as estimated from XRD measurements, the very different temperature of desorption of superoxide between rods and particles may imply that the strain is not the only factor affecting the lowering of the desorption temperature for the rods. Indeed, rods have been found to have higher concentrations of surface vacancy clusters that can adsorb a large amount of oxygen, compared to particles and cubes.[77] Although not directly comparable, the desorption temperatures for our oxygen species (in our case, it is peroxide H/OO/H) are 270, 361 and 574 K from stoichiometric, and 593, 568 and 751 K from oxygen-deficient {111}, {110} and {100} unstrained surfaces at a partial pressure of 10^{-12} bar. On the other hand, for 2% tensile strain, the desorption temperatures for the oxygen species are 337, 398 and 640 K from stoichiometric, and 580, 564 and 752 K from oxygen deficient {111}, {110} and {100} strained surfaces at a partial pressure of 10^{-12} bar. This demonstrates that strain has a bigger effect on stoichiometric than oxygen-deficient surfaces.

The temperatures of desorption for all configurations are provided in Fig. S4 and S5;† here, for each surface, the effect of strain on T_{D,H_2O_2} is visualized as a change in desorption temperature, $\Delta T_{D,(p_{H2}O_2)}$ (eqn (7)), with reference to the T_D of the unstrained $T^{Z,0\%}_{D,(p_{H_2O_2})}$ and strained $T^{Z,strain\%}_{D,(p_{H_2O_2})}$ surfaces at a specific partial pressure of H_2O_2 ($p_{H_2O_2}$).

$$\Delta T_{D,(p_{H_2O_2})} = T^{Z,0\%}_{D,(p_{H_2O_2})} - T^{Z,strain\%}_{D,(p_{H_2O_2})} \quad (7)$$

A $\Delta T_{D,(p_{H2}O_2)} < 0$ implies that the H_2O_2 species is more strongly adsorbed on strained than unstrained CeO_2 as $T^{Z,strain\%}_{D,(p_{H_2O_2})} > T^{Z,0\%}_{D,(p_{H_2O_2})}$. The opposite applies for $\Delta T_{D,(p_{H2}O_2)} > 0$.

Under tensile strain, a negative change in the adsorption of hydrogen peroxide species is observed at all stoichiometric surfaces (Fig. 3C(I–IV)), with the only exceptions for 2% and 4%_{110}S-H_2O_2 at $p_{H_2O_2}$ = −12.5 (Fig. 3C(II and IV)). On the other hand, increasing compressive strain results in a positive $\Delta T_{D,(p_{H2}O_2)}$, with a few exceptions for molecular H_2O_2 (−2% and −4%_{110}S-H_2O_2 at $p_{H_2O_2}$ = 0 (Fig. 3C(V and VII)), and dissociatively adsorbed H_2O_2 (−4%_{100}S-HO/OH at $p_{H_2O_2}$ = −12.5/0, −4%_{100}S-H/OO/H at $p_{H_2O_2}$ = −12.5/0 (Fig. 3C(VII and VIII)), −2%_{100}S-H/OO/H at $p_{H_2O_2}$ = 0 (Fig. 3C(VI)).

On an oxygen-deficient surface, $\Delta T_{D,(p_{H2}O_2)}$ (Fig. 3D) is generally relatively small, either positive or negative, for both tensile and compressive strain values. The difference in desorption temperature between unstrained and strained oxygen-deficient surfaces is less compared to that of stoichiometric surfaces, where we observe a higher $\Delta T_{D,(p_{H2}O_2)}$, when strain is applied, either compressive or tensile. The reason is that oxygen-deficient surfaces are less affected by strain, as oxygen vacancies and Ce^{3+} produce a more distorted lattice, which can accommodate strain more easily compared to stoichiometric surfaces. The surface energy of oxygen-deficient (Fig. 1F) is lower than that of stoichiometric surfaces (Fig. 1E).

3.4. Morphology

Here, we focus on the morphology of nanoparticles at room temperature (298 K) and 1 bar partial pressure of hydrogen peroxide. Each nanoparticle has a specific ratio of the three surfaces, *i.e.*, {100}:{110}:{111}, as well as their surface composition, whether bare (B) or adsorbed (A) with H_2O_2 species. The shape of the nanoparticles is governed by the ratio of the surfaces. For this reason, we also present surface area phase diagrams that represent the ratio amongst the surfaces as a function of pressure and temperature (Fig. S6–S11†).[40,47,52,106]

For each morphology presented in Fig. 4, the ratio of surfaces {100}:{110}:{111} is presented alongside the surface composition of bare unstrained and strained stoichiometric and oxygen-deficient surfaces. When considering bare surfaces, either stoichiometric (Fig. 4A) or oxygen-deficient (Fig. 4B), the {111} surface dominates all morphologies of CeNPs, at any compressive and tensile strains. Some {110} edges appear at higher tensile-strained stoichiometric nanoparticles and higher compressively strained oxygen-deficient nanoparticles.

The morphologies of strained surfaces in the presence of dissociatively and molecularly adsorbed H_2O_2 at room temperature and pressure (298 K, 1 bar) are shown in Fig. 5. The octahedral morphology is consistently observed in nearly all tensile and compressive strains, regardless of whether the

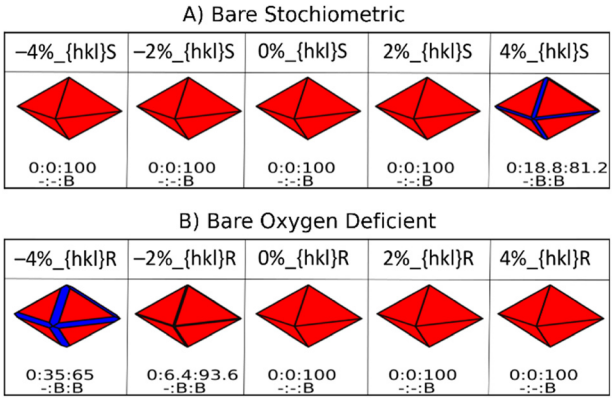

Fig. 4 The shape of CeO_2 unstrained and strained bare nanoparticles. Red, blue and green represent the {111}, {110} and {100} CeO_2 surfaces, respectively. The shapes of the nanoparticles are generated at a hydrogen peroxide partial pressure of 1 bar and 298 K using the Wulff construction routines in Pymatgen.[101] Each shape is characterized by a ratio of surfaces defined in numerical percentage ({100} : {110} : {111}). The label B defines a bare surface. The shape of the stoichiometric nanoparticles is redrawn from our previous work.[40]

surfaces of nanoparticles are adsorbed or bare. As the temperature rises from 298 to 673 K (Fig. S13–S17†), no notable variations in the octahedral shape of the nanoparticles are evident. At tensile strains reaching 4%, stoichiometric nanoparticles begin to exhibit {110} edges and {100} facets (Fig. 5A). In contrast, oxygen-deficient nanoparticles do not display this behaviour, except for the case of H_2O_2 molecularly adsorbed nanoparticles under tensile strain, where the {110} surface becomes dominant, resulting in a transformation of the shape from octahedral to rhombic dodecahedron (Fig. 5B). Increasing temperature does not have much of an effect on the morphologies of stoichiometric and oxygen deficient nanoparticles, which retain the octahedral shape (Fig. S12–S16†).

The regulation of nanoparticle geometries is essential, as different shapes display unique surface properties that lead to varying activities and, as a result, a range of functionalities. Cerium oxide shows peroxidase activity (POD), however the effect of strain on POD activity has not yet been reported.

In a strained ultrathin CeO_2 nanoplate with inherent 3.0% in-plane and 10.0% out-of-plane tensile strain, this induces a tetragonal distortion, which enhances the covalency of the Ce–O bond and results in approximately a 2.6-fold increase in superoxide dismutase SOD activity when compared to unstrained CeNPs.[32] Thus, it is very plausible that strain can be used to tune POD activity.

There is a consensus that octahedral nanoparticles are relatively inactive in terms of POD. However, polyhedral nanoparticles expressing the {111} surface (8–14 nm) display POD activity towards the oxidation of TMB·2HCl in the presence of H_2O_2, much higher than that of the natural enzyme.[18] This suggests that the {111} surface is still active or receptive to interact with hydrogen peroxide. Nonetheless, since the surface adsorption of H_2O_2 by ceria is the rate-limiting step of the POD reaction, it is possible that the {111} surface may not exhibit optimal performance. Indeed, the affinity of the {100} surfaces towards H_2O_2 was confirmed to be ~18 and ~9 times higher than that of the {110} and {111} surfaces,[69] respectively, and rods exposing more {111} tip surfaces were unable to activate H_2O_2 effectively.[102]

There are conflicting reports suggesting that cubes or rods exhibit greater activity.

Different reports display that cubes (15–60 nm, Ce^{4+}/Ce^{3+} ratio = 3.94) expressing the {100} surface display higher POD activity than rods (expressing the {110} surface, lengths 200 nm/diameter 10 nm, Ce^{4+}/Ce^{3+} ratio = 5.07) and octahedra (expressing the {111} surface, 20 nm, Ce^{4+}/Ce^{3+} ratio = 10.03), which are 325% and 1133% less active, respectively.[69] Nanocubes (31.2% of Ce^{3+}, 13 nm) were found 23 times more POD active than nanorods (31.2% of Ce^{3+}, 10 nm).[103] POD activity has also been found for larger particles with cubes ({100}, 15–45 nm) displaying 3.6 times higher activity than rods ({110}, 10 nm with a length up to 350 nm) and 23 times higher than octahedra ({111}, 17 nm).[87]

However, other reports have found that rods are more active than cubes. Nanorods ({110}/{111}, Ce^{3+} = 20.0%, Vo = 39.9%) show the highest POD activity (3.5 times higher than cubes (Ce^{3+} = 13.4%, Vo = 28.8%), with nanooctahedra (Ce^{3+} = 10.7%, Vo = 26.9%) almost inactive) due to their highest H_2O_2 substrate affinity and fastest reaction rate as compared to nanocube and nanoctahedra.[104] Porous ceria nanorods (diameter 8 nm, length ~60 nm, pore size 2–4 nm, Ce^{3+} = 32.8%) have been found with a catalytic constant for POD-like activity 8.4 times higher than non-porous nanorods (Ce^{3+} = 14.4%). The largest surface area and highest surface Ce^{3+} fraction of the porous ceria nanorod is likely to have provided the most catalytic sites, resulting in the strongest POD activity compared to that of other non-porous nanorods.[105] Any reduction of the lateral {110} surfaces on rods led to a significant decrease in POD activity, while enhancing the surface area of {110} surfaces increased POD activity by 1.86-fold.[102]

Although it is clear from the literature findings that octahedral nanoparticles are the least active towards POD activity as they express the {111} surface, which appear to be the one with less affinity towards hydrogen peroxide, from a thermodynamic point of view, our data indicates that the adsorption of any hydrogen peroxide or its dissociative products is not sufficient to shift the equilibrium towards more active morphologies (*i.e.*, cubes and rods). Our morphologies do not include any information on kinetics, which should be a focus of future studies. However, during the lifespan of the materials in operation, a thermodynamic driving force exists for the reconstruction of nanoparticles (due to external conditions of temperature and pressure), and our data show that this reconstruction can enable the nanoparticles to stabilize the less active octahedral shapes. Strain does not affect the morphology of the nanoparticles

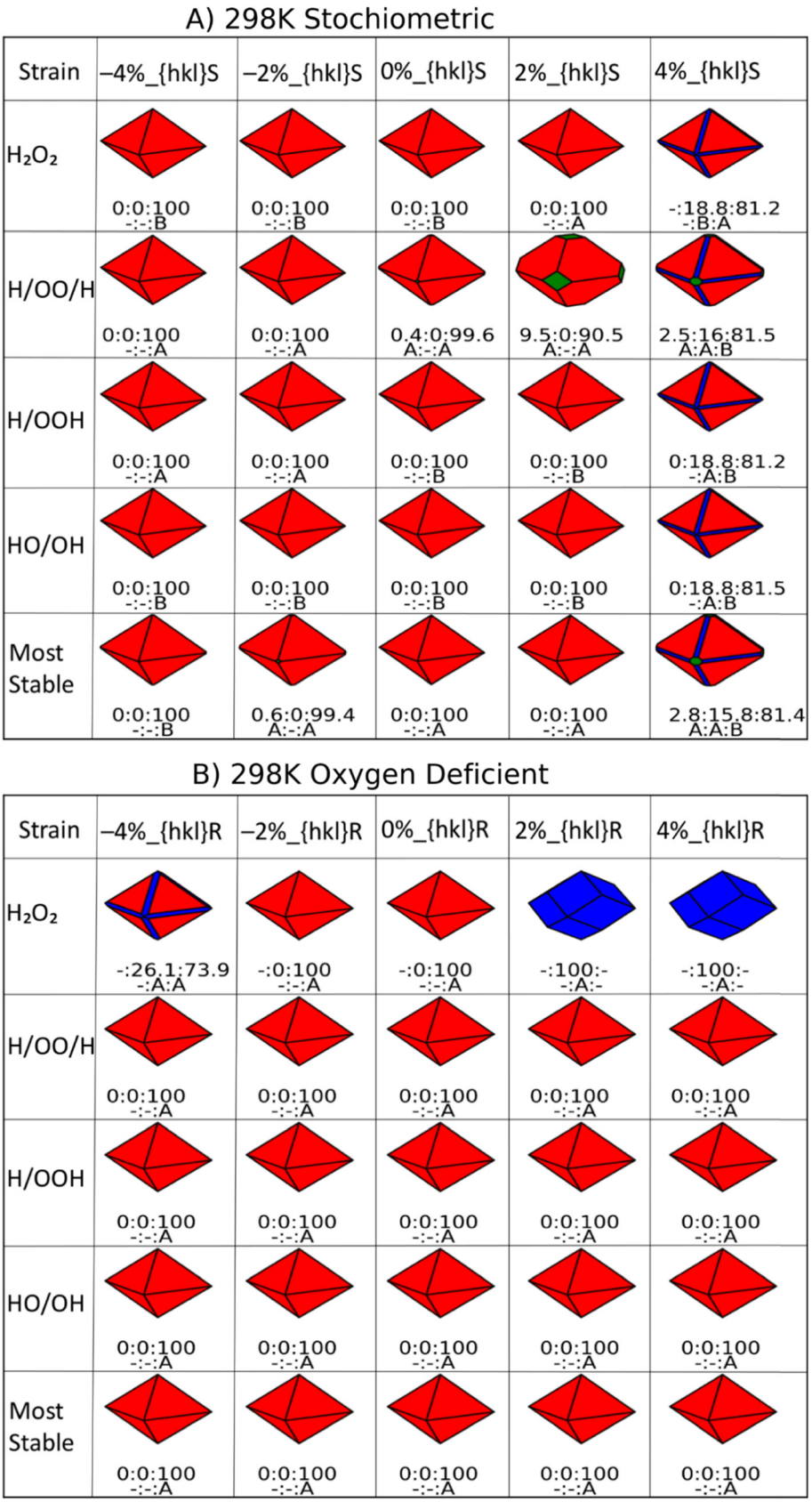

Fig. 5 CeO_2 nanoparticle shapes of dissociatively and associatively adsorbed hydrogen peroxide on CeO_2 {100}, {110} and {111} surfaces. Red, blue and green represent the {111}, {110} and {100} CeO_2 surfaces, respectively. The nanoparticle shapes are generated at 1 bar and 298 K. Each shape is characterized by a ratio of surfaces defined in numerical percentage ({100} : {110} : {111}). The label B defines a bare surface and A means adsorbed.

(Fig. 5), although it changes the adsorption energies of H_2O_2 and its derivatives significantly (Fig. 2). This was not the case for hydrated nanoparticles, where cuboidal nanoparticles could be stabilized.[40] Certainly, future modelling studies should prioritize the competitive adsorption of adsorbates such as water; however, these developments are not without their practical challenges and beyond the scope of this research.[49,106] The only significant shift in morphology is observed for tensile-strained oxygen-deficient nanoparticles (Fig. 5B), where the {110} surface dominates the morphology, and the nanoparticle assumes a rhombic dodecahedral shape. However, as the adsorption energies of H_2O_2 on oxygen-deficient surfaces, including the {110} (Fig. 2), are the least stable compared to the adsorption of hydroxyl, peroxide, hydroperoxide and superoxide, then it will be unlikely that this shape can form.

Conclusion

In this study, we conducted *ab initio* calculations to assess the energetics of both strained and unstrained stoichiometric and oxygen-deficient CeO_2 {100}, {110}, and {111} surfaces during the adsorption of hydrogen peroxide and its dissociation products.

The order of reducibility of bare CeO_2 surfaces is {110} > {100} > {111}. It becomes easier to reduce surfaces under tensile strain than compressive strain as the lattice can more easily accommodate the larger Ce^{3+} ions under tensile strain.

When strained and unstrained surfaces interact with hydrogen peroxide and its dissociation products, we observe that the adsorption energy is generally stabilized on stoichiometric surfaces, whereas it is destabilized on oxygen-deficient surfaces upon tensile strain. Salient findings from this adsorption study are:

1) Molecular H_2O_2 tends to be unstable and therefore dissociates on the oxygen-deficient {100} surface, but also under tensile strain on the oxygen-deficient {111} surface;

2) OH radicals are unstable on the stoichiometric unstrained and strained {111} surfaces. OH radicals are unstable on all oxygen-deficient, strained and unstrained surfaces as they are converted into OH anions *via* an electron transfer from the surface Ce^{3+}; at this point, the adsorption of the anionic species is stable.

3) The peroxide species generated by the dissociation, H/OO/H, is not always the most stable species on all strained and unstrained, stoichiometric and reduced surfaces. On the stoichiometric {111} surface, we observe the formation of molecular O_2. The superoxide is generally unstable on our surfaces except for tensile-strained oxygen-deficient {111}, and stoichiometric and oxygen-deficient {100} surfaces.

We find that the adsorption stability of molecular H_2O_2 on unstrained stoichiometric surfaces follows the order {110}S > {100}S > {111}S, which remains unchanged upon compressive and tensile strains. The adsorption stability for dissociated states on stoichiometric surfaces is {100}S > {110}S > {111}S, while on oxygen-deficient surfaces, the order follows {100}R > {111}R > {110}R. This provides clarity on the behavior of oxygen species on ceria, demonstrating how surface strain and facet morphology influence the relative stability of the anchoring of hydrogen peroxide and its dissociation products on ceria surfaces. Indeed, one of the limiting steps for POD activity is the interaction of the substrate with the ceria surfaces. The {111} surface would therefore not be ideal for promoting POD activity.

This was followed by a thermodynamic approach to calculate the desorption temperatures of adsorbed species on strained surfaces and determine the surface composition and particle morphology of strained ceria surfaces, as a function of temperature and partial pressure of hydrogen peroxide.

The applied thermodynamic approach facilitates the assessment of the desorption temperature of hydrogen peroxide and its dissociation products on strained surfaces, while also contributing to the definition of nanoparticle morphology under specific environmental conditions. Our findings indicate a thermodynamic driving force towards octahedral morphologies across all strains for every adsorbed species at room temperature, except in the case of oxygen-deficient nanoparticles, where the {110} surface is the most prevalent. Increasing temperatures have minimal impact on the morphologies, which continue to maintain their octahedral shape.

As the ability to manipulate the shapes of nanoparticles can result in varied functionalities, which is essential for numerous applications of ceria, our methodology provides a simple approach that can be broadly applied to predict the effect of strain on particle morphologies of materials and minerals under relevant environmental conditions. Future developments of our thermodynamic model for studying the interaction of hydrogen peroxide and ceria surfaces should account for the effects of coverage, the inclusion of the aqueous medium, as well as pH and kinetics effects.

Data availability

Data related to this research are available at **https://doi.org/10.17632/4fh372cgdy**.

Author contributions

SM, KMT, TS, MM: formal analysis, investigation, visualization, and writing – original draft. MM, DJC, LJG: conceptualization, methodology, validation, resources, and data curation, supervision, project administration, and funding acquisition. SM, KMT, TS, DJC, LJG, MM: writing – review and editing.

Conflicts of interest

There is no conflict of interest among the authors.

Acknowledgements

Simulations were run on ARCHER2 UK National Supercomputing Services *via* our membership of the UK HEC

Materials Chemistry Consortium (HEC MCC) funded by the EPSRC (EP/X035859/1). Analysis was performed using the Orion computing facility and the Violeta HPC at the University of Huddersfield. KMT was funded *via* the Vice Chancellor's Scholarship Scheme at the University of Huddersfield. TS was funded by the University of Huddersfield (UoH) EPSRC-DTP competition 2018–19 (EP/R513234/1).

References

1 A. Trovarelli and J. Llorca, Ceria Catalysts at Nanoscale: How Do Crystal Shapes Shape Catalysis?, *ACS Catal.*, 2017, **7**, 4716–4735.
2 N. Farooq, Z. ur Rehman, M. I. Khan, W. Iman, I. Kanwal, S. Khan, A. Shanableh, S. Manzoor and R. Luque, A comprehensive review on ceria based materials for environmental-related applications, *Inorg. Chem. Commun.*, 2024, **170**, 113086.
3 M. Nadeem, R. Khan, K. Afridi, A. Nadhman, S. Ullah, S. Faisal, Z. U. Mabood, C. Hano and B. H. Abbasi, Green Synthesis of Cerium Oxide Nanoparticles (CeO_2 NPs) and Their Antimicrobial Applications: A Review, *Int. J. Nanomed.*, 2020, **15**, 5951–5961.
4 C. Xu and X. Qu, Cerium Oxide Nanoparticle: A Remarkably Versatile Rare Earth Nanomaterial For Biological Applications, *NPG Asia Mater.*, 2014, **6**, e90–e90.
5 S. Rajeshkumar and P. Naik, Synthesis And Biomedical Applications Of Cerium Oxide Nanoparticles – A Review, *Biotechnol. Rep.*, 2018, **17**, 1–5.
6 Y. G. Kim, Y. Lee, N. Lee, M. Soh, D. Kim and T. Hyeon, Ceria-Based Therapeutic Antioxidants for Biomedical Applications, *Adv. Mater.*, 2024, **36**, 2210819.
7 I. Celardo, J. Z. Pedersen, E. Traversa and L. Ghibelli, Pharmacological potential of cerium oxide nanoparticles, *Nanoscale*, 2011, **3**, 1411–1420.
8 C. Walkey, S. Das, S. Seal, J. Erlichman, K. Heckman, L. Ghibelli, E. Traversa, J. F. McGinnis and W. T. Self, Catalytic Properties And Biomedical Applications Of Cerium Oxide Nanoparticles, *Environ. Sci.: Nano*, 2015, **2**, 33–53.
9 A. Othman, A. Gowda, D. Andreescu, M. H. Hassan, S. V. Babu, J. Seo and S. Andreescu, Two Decades Of Ceria Nanoparticle Research: Structure, Properties And Emerging Applications, *Mater. Horiz.*, 2024, **11**, 3213–3266.
10 C. Korsvik, S. Patil, S. Seal and W. T. Self, Superoxide Dismutase Mimetic Properties Exhibited By Vacancy Engineered Ceria Nanoparticles, *Chem. Commun.*, 2007, 1056–1058.
11 T. Montini, M. Melchionna, M. Monai and P. Fornasiero, Fundamentals and Catalytic Applications of CeO_2-Based Materials, *Chem. Rev.*, 2016, **116**, 5987–6041.
12 X. Liu, J. Wu, Q. Liu, A. Lin, S. Li, Y. Zhang, Q. Wang, T. Li, X. An and Z. Zhou, *et al.*, Synthesis-temperature-regulated multi-enzyme-mimicking activities of ceria nanozymes, *J. Mater. Chem. B*, 2021, **9**, 7238–7245.
13 Y. Huang, J. Ren and X. Qu, Nanozymes: Classification, Catalytic Mechanisms, Activity Regulation, and Applications, *Chem. Rev.*, 2019, **119**, 4357–4412.
14 J. Wu, X. Wang, Q. Wang, Z. Lou, S. Li, Y. Zhu, L. Qin and H. Wei, Nanomaterials With Enzyme-Like Characteristics (Nanozymes): Next-Generation Artificial Enzymes (II), *Chem. Soc. Rev.*, 2019, **48**, 1004–1076.
15 S. S. Lee, W. Song, M. Cho, H. L. Puppala, P. Nguyen, H. Zhu, L. Segatori and V. L. Colvin, Antioxidant Properties of Cerium Oxide Nanocrystals as a Function of Nanocrystal Diameter and Surface Coating, *ACS Nano*, 2013, **7**, 9693–9703.
16 T. Pirmohamed, J. M. Dowding, S. Singh, B. Wasserman, E. Heckert, A. S. Karakoti, J. E. S. King, S. Seal and W. T. Self, Nanoceria Exhibit Redox State-Dependent Catalase Mimetic Activity, *Chem. Commun.*, 2010, **46**, 2736–2738.
17 Y. Wu, L. Yang, Q. Wu, Q. Liu, L. Zou, X. Yang and K. Tang, Regulation of the Oxidase Mimetic Activity of Ceria Nanoparticles by Buffer Composition, *Chem. – Eur. J.*, 2023, **29**, e202204071.
18 X. Jiao, H. Song, H. Zhao, W. Bai, L. Zhang and Y. Lv, Well-redispersed ceria nanoparticles: Promising peroxidase mimetics for H_2O_2 and glucose detection, *Anal. Methods*, 2012, **4**, 3261–3267.
19 E. G. Heckert, A. S. Karakoti, S. Seal and W. T. Self, The Role Of Cerium Redox State In The SOD Mimetic Activity Of Nanoceria, *Biomaterials*, 2008, **29**, 2705–2709.
20 Z. Tian, H. Liu, Z. Guo, W. Gou, Z. Liang, Y. Qu, L. Han and L. Liu, A PH-Responsive Polymer-CeO_2 Hybrid To Catalytically Generate Oxidative Stress For Tumor Therapy, *Small*, 2020, **16**, 2004654.
21 K. M. Ta, C. J. Neal, M. Coathup, S. Seal, L. J. Gillie, D. J. Cooke, S. C. Parker and M. Molinari, The Buffering Activity of Ceria toward Reactive Oxygen Species: A Density Functional Theory Perspective, *J. Phys. Chem. C*, 2025, **129**, 11989–12005.
22 M. Valko, D. Leibfritz, J. Moncol, M. T. D. Cronin, M. Mazur and J. Telser, Free Radicals And Antioxidants In Normal Physiological Functions And Human Disease, *Int. J. Biochem. Cell Biol.*, 2007, **39**, 44–84.
23 F. Wei, C. J. Neal, T. S. Sakthivel, Y. Fu, M. Omer, A. Adhikary, S. Ward, K. M. Ta, S. Moxon and M. Molinari, *et al.*, A Novel Approach For The Prevention Of Ionizing Radiation-Induced Bone Loss Using A Designer Multifunctional Cerium Oxide Nanozyme, *Bioact. Mater.*, 2023, **21**, 547–565.
24 A. S. Pugazhendhi, C. J. Neal, K. M. Ta, M. Molinari, U. Kumar, F. Wei, E. Kolanthai, A. Ady, C. Drake and M. Hughes, *et al.*, A Neoteric Antibacterial Ceria-Silver Nanozyme For Abiotic Surfaces, *Biomaterials*, 2024, **307**, 122527.
25 B. Liu, Z. Sun, P.-J. J. Huang and J. Liu, Hydrogen Peroxide Displacing DNA from Nanoceria: Mechanism and Detection of Glucose in Serum, *J. Am. Chem. Soc.*, 2015, **137**, 1290–1295.
26 B. Lipinski, Hydroxyl radical and its scavengers in health and disease, *Oxid. Med. Cell. Longevity*, 2011, **2011**, 809696.

27 Z. Wang, X. Shen and X. Gao, Density Functional Theory Mechanistic Insight into the Peroxidase- and Oxidase-like Activities of Nanoceria, *J. Phys. Chem. C*, 2021, **125**, 23098–23104.
28 S. Deshpande, S. Patil, S. V. N. T. Kuchibhatla and S. Seal, Size dependency variation in lattice parameter and valency states in nanocrystalline cerium oxide, *Appl. Phys. Lett.*, 2005, **87**, 133113.
29 D. S. Tsvetkov, V. V. Sereda, D. A. Malyshkin, I. L. Ivanov and A. Y. Zuev, Chemical Lattice Strain In Nonstoichiometric Oxides: An Overview, *J. Mater. Chem. A*, 2022, **10**, 6351–6375.
30 M. Soh, D.-W. Kang, H.-G. Jeong, D. Kim, D. Y. Kim, W. Yang, C. Song, S. Baik, I.-Y. Choi and S.-K. Ki, *et al.*, Ceria–Zirconia Nanoparticles as an Enhanced Multi-Antioxidant for Sepsis Treatment, *Angew. Chem., Int. Ed.*, 2017, **56**, 11399–11403.
31 G. Vinothkumar, S. Rengaraj, P. Arunkumar, S. W. Cha and K. Suresh Babu, Ionic Radii and Concentration Dependency of RE^{3+} (Eu^{3+}, Nd^{3+}, Pr^{3+}, and La^{3+})-Doped Cerium Oxide Nanoparticles for Enhanced Multienzyme-Mimetic and Hydroxyl Radical Scavenging Activity, *J. Phys. Chem. C*, 2019, **123**, 541–553.
32 C. Liu, L. Gui, J.-J. Zheng, Y.-Q. Xu, B. Song, L. Yi, Y. Jia, A. Taledaohan, Y. Wang and X. Gao, *et al.*, Intrinsic Strain-Mediated Ultrathin Ceria Nanoantioxidant, *J. Am. Chem. Soc.*, 2023, **145**, 19086–19097.
33 Y. Sun, L. Xu, X. Liu, Y. Shen, Y. Zhang, N. Gu and F. Xiong, Coronal Relay Reactor Fe_3O_4@CeO_2 for Accelerating Ros Axial Conversion Through Enhanced Enzyme-Like Effect And Relay Effect, *Chem. Eng. J.*, 2022, **429**, 132303.
34 L. Artiglia, S. Agnoli, M. C. Paganini, M. Cattelan and G. Granozzi, TiO_2@CeO_x Core–Shell Nanoparticles as Artificial Enzymes with Peroxidase-Like Activity, *ACS Appl. Mater. Interfaces*, 2014, **6**, 20130–20136.
35 X. Wang, D. Liu, J. Li, J. Zhen and H. Zhang, Clean synthesis of Cu_2O@CeO_2 core@shell nanocubes with highly active interface, *NPG Asia Mater.*, 2015, **7**, e158–e158.
36 D. Jampaiah, T. Srinivasa Reddy, V. E. Coyle, A. Nafady and S. K. Bhargava, Co_3O_4@CeO_2 Hybrid Flower-Like Microspheres: A Strong Synergistic Peroxidase-Mimicking Artificial Enzyme With High Sensitivity For Glucose Detection, *J. Mater. Chem. B*, 2017, **5**, 720–730.
37 L. Deng, C. Chen, C. Zhu, S. Dong and H. Lu, Multiplexed Bioactive Paper Based On GO@SiO_2@CeO_2 Nanosheets For A Low-Cost Diagnostics Platform, *Biosens. Bioelectron.*, 2014, **52**, 324–329.
38 S. Bhagat, N. V. Srikanth Vallabani, V. Shutthanandan, M. Bowden, A. S. Karakoti and S. Singh, Gold Core/Ceria Shell-Based Redox Active Nanozyme Mimicking The Biological Multienzyme Complex Phenomenon, *J. Colloid Interface Sci.*, 2018, **513**, 831–842.
39 T. Shokuhfar, G. K. Arumugam, P. A. Heiden, R. S. Yassar and C. Friedrich, Direct Compressive Measurements of Individual Titanium Dioxide Nanotubes, *ACS Nano*, 2009, **3**, 3098–3102.
40 S. Munir, K. M. Ta, T. Smith, L. J. Gillie, D. J. Cooke, S. C. Parker and M. Molinari, Strain Effects on the Adsorption of Water on Cerium Dioxide Surfaces and Nanoparticles: A Modeling Outlook, *J. Phys. Chem. C*, 2024, **128**, 18451–18464.
41 H. T. Chen, Y. M. Choi, M. Liu and M.-C. Lin, A Theoretical Study of Surface Reduction Mechanisms of CeO_2 (111) and (110) by H_2, *ChemPhysChem*, 2007, **8**, 849–855.
42 K. M. Ta, D. J. Cooke, L. J. Gillie, S. C. Parker, S. Seal, P. B. Wilson, R. M. Phillips, J. M. Skelton and M. Molinari, Infrared and Raman Diagnostic Modeling of Phosphate Adsorption on Ceria Nanoparticles, *J. Phys. Chem. C*, 2023, 20183–20193.
43 G. Kresse and J. Furthmüller, Efficiency Of Ab-Initio Total Energy Calculations for Metals and Semiconductors Using A Plane-Wave Basis Set, *Comput. Mater. Sci.*, 1996, **6**, 15–50.
44 S. L. Dudarev, G. A. Botton, S. Y. Savrasov, C. Humphreys and A. P. Sutton, Electron-Energy-Loss Spectra and the Structural Stability of Nickel Oxide: An LSDA+ U Study, *Phys. Rev. B*, 1998, **57**, 1505.
45 M. Molinari, S. C. Parker, D. C. Sayle and M. S. Islam, Water Adsorption and Its Effect on the Stability of Low Index Stoichiometric and Reduced Surfaces of Ceria, *J. Phys. Chem. C*, 2012, **116**, 7073–7082.
46 A. R. Symington, R. M. Harker, M. T. Storr, M. Molinari and S. C. Parker, Thermodynamic Evolution of Cerium Oxide Nanoparticle Morphology Using Carbon Dioxide, *J. Phys. Chem. C*, 2020, **124**, 23210–23220.
47 A. R. Symington, M. Molinari, S. Moxon, J. M. Flitcroft, D. C. Sayle and S. C. Parker, Strongly Bound Surface Water affects the Shape Evolution of Cerium Oxide Nanoparticles, *J. Phys. Chem. C*, 2020, **124**, 3577–3588.
48 K. M. Ta, D. J. Cooke, L. J. Gillie, S. C. Parker, S. Seal, P. B. Wilson, R. M. Phillips, J. M. Skelton and M. Molinari, Infrared and Raman Diagnostic Modeling of Phosphate Adsorption on Ceria Nanoparticles, *J. Phys. Chem. C*, 2023, **127**, 20183–20193.
49 T. Smith, S. Moxon, J. Tse, J. Skelton, D. Cooke, L. Gillie, E. Silva, R. Harker, M. Storr and S. Parker, *et al.*, Structural Dynamics Of Schottky And Frenkel Defects In CeO_2: A Density-Functional Theory Study, *JPhys Energy*, 2023, **5**, 025004.
50 N. Anwar, R. M. Harker, M. T. Storr, M. Molinari and C.-K. Skylaris, Linear-Scaling Density Functional Theory (DFT) Simulations Of Point, Frenkel And Schottky Defects In CeO_2, *Comput. Mater. Sci.*, 2023, **229**, 112396.
51 M. Molinari, A. R. Symington, D. C. Sayle, T. S. Sakthivel, S. Seal and S. C. Parker, Computer-Aided Design of Nanoceria Structures as Enzyme Mimetic Agents: The Role of Bodily Electrolytes on Maximizing Their Activity, *ACS Appl. Bio Mater.*, 2019, **2**, 1098–1106.
52 S. Moxon, A. Symington, J. Tse, J. Flitcroft, J. Skelton, L. Gillie, D. Cooke, S. Parker and M. Molinari, Composition-Dependent Morphologies of CeO_2 Nanoparticles in the Presence of Co-Adsorbed H_2O and CO_2: A Density Functional Theory Study, *Nanoscale*, 2024, **16**, 11232–11249.

53 G. W. Watson, E. Toby Kelsey, N. H. de Leeuw, D. J. Harris and S. C. Parker, Atomistic Simulation of Dislocations, Surfaces and Interfaces in MgO, *J. Chem. Soc., Faraday Trans.*, 1996, **92**, 433–438.
54 P. M. Oliver, S. C. Parker and W. C. Mackrodt, Computer Simulation of the Crystal Morphology Of NiO, *Modell. Simul. Mater. Sci. Eng.*, 1993, **1**, 755.
55 P. M. Oliver, G. W. Watson and S. C. Parker, Molecular-Dynamics Simulations Of Nickel Oxide Surfaces, *Phys. Rev. B*, 1995, **52**, 5323–5329.
56 M. Capdevila-Cortada and N. López, Entropic contributions enhance polarity compensation for CeO_2(100) surfaces, *Nat. Mater.*, 2017, **16**, 328–334.
57 J. P. Allen and G. W. Watson, Occupation matrix control of d- and f-electron localisations using DFT + U, *Phys. Chem. Chem. Phys.*, 2014, **16**, 21016–21031.
58 F. P. Rotzinger, J. M. Kesselman-Truttmann, S. J. Hug, V. Shklover and M. Grätzel, Structure and Vibrational Spectrum of Formate and Acetate Adsorbed from Aqueous Solution onto the TiO_2 Rutile (110) Surface, *J. Phys. Chem. B*, 2004, **108**, 5004–5017.
59 T. Wu, T. Vegge and H. A. Hansen, Improved Electrocatalytic Water Splitting Reaction on CeO_2(111) by Strain Engineering: A DFT+U Study, *ACS Catal.*, 2019, **9**, 4853–4861.
60 Z.-K. Han, L. Zhang, M. Liu, M. V. Ganduglia-Pirovano and Y. Gao, The Structure Of Oxygen Vacancies In The Near-Surface Of Reduced CeO_2 (111) Under Strain, *Front. Chem.*, 2019, **7**, 436.
61 Z. Liu, B. Wang and C. Cazorla, Mechanical And Electronic Properties of CeO_2 Under Uniaxial Tensile Loading: A DFT Study, *Materialia*, 2021, **15**, 101050.
62 D. Ma, Z. Lu, Y. Tang, T. Li, Z. Tang and Z. Yang, Effect Of Lattice Strain on the Oxygen Vacancy Formation and Hydrogen Adsorption at CeO_2(111) Surface, *Phys. Lett. A*, 2014, **378**, 2570–2575.
63 J. V. Kildgaard, H. A. Hansen and T. Vegge, DFT+ U Study of Strain-Engineered CO_2 Reduction on a CeO_{2-x} (111) Facet, *J. Phys. Chem. C*, 2021, **125**, 14221–14227.
64 T. Wu, N. López, T. Vegge and H. A. Hansen, Facet-Dependent Electrocatalytic Water Splitting Reaction On CeO_2: A DFT + U study, *J. Catal.*, 2020, **388**, 1–10.
65 M. Nolan, S. C. Parker and G. W. Watson, The Electronic Structure Of Oxygen Vacancy Defects At The Low Index Surfaces Of Ceria, *Surf. Sci.*, 2005, **595**, 223–232.
66 D. S. Aidhy, B. Liu, Y. Zhang and W. Weber, Strain-Induced Phase And Oxygen-Vacancy Stability In Ionic Interfaces From First-Principles Calculations, *J. Phys. Chem. C*, 2014, **118**, 30139–30144.
67 O. Matz and M. Calatayud, Breaking H_2 with CeO_2: Effect of Surface Termination, *ACS Omega*, 2018, **3**, 16063–16073.
68 L. Brugnoli, S. Urata and A. Pedone, H_2O_2 Adsorption And Dissociation On Various CeO_2 (111) Surface Models: A First-Principles Study, *J. Phys.: Condens. Matter*, 2022, **34**, 164006.
69 Z. Tan, Y.-C. Chen, J. Zhang, J.-P. Chou, A. Hu and Y.-K. Peng, Nanoisozymes: The Origin behind Pristine CeO_2 as Enzyme Mimetics, *Chem. – Eur. J.*, 2020, **26**, 10598–10606.
70 L. E. B. Lucchetti, J. M. de Almeida, P. A. S. Autreto and M. C. Santos, Assessing the oxygen reduction reaction by a 2-electron mechanism on ceria surfaces, *Phys. Chem. Chem. Phys.*, 2021, **23**, 18580–18587.
71 Y.-C. Zhang, Y.-K. Liu, L. Zhang, E. Xiu-tian-feng, L. Pan, X. Zhang, Fazal-e-Aleem, D.-R. Zou, S.-H. Liu and J.-J. Zou, DFT Study On Water Oxidation On Nitrogen-Doped Ceria Oxide, *Appl. Surf. Sci.*, 2018, **452**, 423–428.
72 R. Lawler, J. Cho, H. C. Ham, H. Ju, S. W. Lee, J. Y. Kim, J. Il Choi and S. S. Jang, CeO_2(111) Surface with Oxygen Vacancy for Radical Scavenging: A Density Functional Theory Approach, *J. Phys. Chem. C*, 2020, **124**, 20950–20959.
73 U. Castanet, C. Feral-Martin, A. Demourgues, R. L. Neale, D. C. Sayle, F. Caddeo, J. M. Flitcroft, R. Caygill, B. J. Pointon and M. Molinari, *et al.*, Controlling the {111}/{110} Surface Ratio of Cuboidal Ceria Nanoparticles, *ACS Appl. Mater. Interfaces*, 2019, **11**, 11384–11390.
74 P. R. L. Keating, D. O. Scanlon, B. J. Morgan, N. M. Galea and G. W. Watson, Analysis of Intrinsic Defects in CeO_2 Using a Koopmans-Like GGA+U Approach, *J. Phys. Chem. C*, 2012, **116**, 2443–2452.
75 Y. M. Choi, H. Abernathy, H.-T. Chen, M. C. Lin and M. Liu, Characterization of O_2–CeO_2 Interactions Using In Situ Raman Spectroscopy and First-Principle Calculations, *ChemPhysChem*, 2006, **7**, 1957–1963.
76 C. Schilling, M. V. Ganduglia-Pirovano and C. Hess, Experimental and Theoretical Study on the Nature of Adsorbed Oxygen Species on Shaped Ceria Nanoparticles, *J. Phys. Chem. Lett.*, 2018, **9**, 6593–6598.
77 L. Wang, Y. Wang, Y. Zhang, Y. Yu, H. He, X. Qin and B. Wang, Shape Dependence Of Nanoceria On Complete Catalytic Oxidation Of O-Xylene, *Catal. Sci. Technol.*, 2016, **6**, 4840–4848.
78 D. Du, J. Kullgren, B. Kocmaruk, K. Hermansson and P. Broqvist, Simulated temperature programmed desorption experiments for nanoceria powders, *J. Catal.*, 2020, **384**, 252–259.
79 M. Huang and S. Fabris, Role of surface peroxo and superoxo species in the low-temperature oxygen buffering of ceria: Density functional theory calculations, *Phys. Rev. B: Condens. Matter*, 2007, **75**, 081404.
80 Y. Zhao, B.-T. Teng, X.-D. Wen, Y. Zhao, Q.-P. Chen, L.-H. Zhao and M.-F. Luo, Superoxide and Peroxide Species on CeO_2(111), and Their Oxidation Roles, *J. Phys. Chem. C*, 2012, **116**, 15986–15991.
81 B.-T. Teng, S.-Y. Jiang, Z.-X. Yang, M.-F. Luo and Y.-Z. Lan, A Density Functional Theory Study Of Formaldehyde Adsorption And Oxidation On CeO_2(111) surface, *Surf. Sci.*, 2010, **604**, 68–78.
82 H.-T. Chen, J.-G. Chang, H.-L. Chen and S.-P. Ju, Identifying The O_2 Diffusion And Reduction Mechanisms On CeO_2 Electrolyte In Solid Oxide Fuel Cells: A DFT+U study, *J. Comput. Chem.*, 2009, **30**, 2433–2442.
83 J. Kullgren, K. Hermansson and P. Broqvist, Reactive oxygen species in stoichiometric ceria: Bulk and low-index surfaces, *Phys. Status Solidi RRL*, 2014, **8**, 600–604.

84 M. Ziemba, M. V. Ganduglia-Pirovano and C. Hess, Elucidating the Oxygen Storage-Release Dynamics in Ceria Nanorods by Combined Multi-Wavelength Raman Spectroscopy and DFT, *J. Phys. Chem. Lett.*, 2020, **11**, 8554–8559.

85 L. Kang, B. Wang, Q. Bing, M. Zalibera, R. Büchel, R. Xu, Q. Wang, Y. Liu, D. Gianolio and C. C. Tang, *et al.*, Adsorption and activation of molecular oxygen over atomic copper(I/II) site on ceria, *Nat. Commun.*, 2020, **11**, 4008.

86 M. Nolan, Healing Of Oxygen Vacancies On Reduced Surfaces Of Gold-Doped Ceria, *J. Chem. Phys.*, 2009, **130**, 144702.

87 B. Yuan, Z. Tan, Q. Guo, X. Shen, C. Zhao, J. L. Chen and Y.-K. Peng, Regulating the H_2O_2 Activation Pathway on a Well-Defined CeO_2 Nanozyme Allows the Entire Steering of Its Specificity between Associated Enzymatic Reactions, *ACS Nano*, 2023, **17**, 17383–17393.

88 J. Tse, M. Molinari, S. C. Parker and A. R. Symington, SurfinPy 2.0: A Phase Diagram Generator for Surfaces and Bulk Phases, *J. Open Source Softw.*, 2022, **7**, 4014.

89 A. R. Symington, J. Tse, M. Molinari, A. Marmier and S. C. Parker, Surfinpy: A Surface Phase Diagram Generator, *J. Open Source Softw.*, 2019, **4**, 1210.

90 M. W. Chase and Organization, N. I. S., *NIST-JANAF thermochemical tables*, American Chemical Society, Washington, DC, 1998, vol. 9.

91 S. M. Bashir and H. Idriss, The reaction of propylene to propylene-oxide on CeO_2: An FTIR spectroscopy and temperature programmed desorption study, *J. Chem. Phys.*, 2020, **152**, 044712.

92 C. Li, K. Domen, K. Maruya and T. Onishi, Dioxygen adsorption on well-outgassed and partially reduced cerium oxide studied by FT-IR, *J. Am. Chem. Soc.*, 1989, **111**, 7683–7687.

93 C. Li, K. Domen, K.-I. Maruya and T. Onishi, Oxygen Exchange Reactions Over Cerium Oxide: An Ft-IR Study, *J. Catal.*, 1990, **123**, 436–442.

94 Y. Zhang, Z. Kang, J. Dong, H. Abernathy and M. Liu, Self-Assembly Of Cerium Compound Nanopetals Via A Hydrothermal Process: Synthesis, Formation Mechanism And Properties, *J. Solid State Chem.*, 2006, **179**, 1733–1738.

95 C. Yang, X. Yu, S. Heißler, P. G. Weidler, A. Nefedov, Y. Wang, C. Wöll, T. Kropp, J. Paier and J. Sauer, O_2 Activation on Ceria Catalysts—The Importance of Substrate Crystallographic Orientation, *Angew. Chem., Int. Ed.*, 2017, **56**, 16399–16404.

96 Z. Wu, M. Li, J. Howe, H. M. Meyer III and S. H. Overbury, Probing Defect Sites on CeO_2 Nanocrystals with Well-Defined Surface Planes by Raman Spectroscopy and O_2 Adsorption, *Langmuir*, 2010, **26**, 16595–16606.

97 D. Du, J. Kullgren, K. Hermansson and P. Broqvist, From Ceria Clusters to Nanoparticles: Superoxides and Supercharging, *J. Phys. Chem. C*, 2019, **123**, 1742–1750.

98 J. Xu, J. Harmer, G. Li, T. Chapman, P. Collier, S. Longworth and S. C. Tsang, Size dependent oxygen buffering capacity of ceria nanocrystals, *Chem. Commun.*, 2010, **46**, 1887–1889.

99 J. Kullgren, K. Hermansson and P. Broqvist, Supercharged Low-Temperature Oxygen Storage Capacity of Ceria at the Nanoscale, *J. Phys. Chem. Lett.*, 2013, **4**, 604–608.

100 N. K. Renuka, N. Harsha and T. Divya, Supercharged ceria quantum dots with exceptionally high oxygen buffer action, *RSC Adv.*, 2015, **5**, 38837–38841.

101 R. Tran, Z. Xu, B. Radhakrishnan, D. Winston, W. Sun, K. Persson and S. Ong, Surface Energies Of Elemental Crystals, *Sci. Data*, 2016, **3**, 160080.

102 T. Cheng, X. Wu, Y. Qiu, B. Yuan, C. Zhao, J. L. Chen and Y.-K. Peng, Spatially Decoupled H_2O_2 Activation Pathways and Multi-Enzyme Activities in Rod-Shaped CeO_2 with Implications for Facet Distribution, *Small*, 2024, **20**, 2401032.

103 Y. Yang, Z. Mao, W. Huang, L. Liu, J. Li, J. Li and Q. Wu, Redox Enzyme-Mimicking Activities Of CeO_2 Nanostructures: Intrinsic Influence Of Exposed Facets, *Sci. Rep.*, 2016, **6**, 35344.

104 M. Chen, X. Zhou, C. Xiong, T. Yuan, W. Wang, Y. Zhao, Z. Xue, W. Guo, Q. Wang and H. Wang, *et al.*, Facet Engineering of Nanoceria for Enzyme-Mimetic Catalysis, *ACS Appl. Mater. Interfaces*, 2022, **14**, 21989–21995.

105 Z. Tian, J. Li, Z. Zhang, W. Gao, X. Zhou and Y. Qu, Highly Sensitive And Robust Peroxidase-Like Activity Of Porous Nanorods Of Ceria And Their Application For Breast Cancer Detection, *Biomaterials*, 2015, **59**, 116–124.

106 S. Moxon, J. M. Flitcroft, L. J. Gillie, D. J. Cooke, J. M. Skelton, S. C. Parker and M. Molinari, Composition-Dependent Morphology Of Stoichiometric And Oxygen Deficient PuO_2 Nanoparticles In The Presence Of H_2O and CO_2: A Density-Functional Theory Study, *Appl. Surf. Sci.*, 2024, **676**, 160997.

